Published in final edited form as:

Cell Rep. 2020 April 07; 31(1): 107477. doi:10.1016/j.celrep.2020.03.041.

Precise Tuning of Cortical Contractility Regulates Cell Shape during Cytokinesis

Nilay Taneja[1], **Matthew R. Bersi**[2], **Sophie M. Baillargeon**[1], **Aidan M. Fenix**[1], **James A. Cooper**[1], **Ryoma Ohi**[3], **Vivian Gama**[1], **W. David Merryman**[2], **Dylan T. Burnette**[1,4,*]

[1]Department of Cell and Developmental Biology, Vanderbilt University, Nashville, TN 37232, USA

[2]Department of Biomedical Engineering, Vanderbilt University, Nashville, TN 37232, USA

[3]Department of Cell and Developmental Biology, University of Michigan, Ann Arbor, MI 48109, USA

[4]Lead Contact

Abstract

SUMMARY—The mechanical properties of the actin cortex regulate shape changes during cell division, cell migration, and tissue morphogenesis. We show that modulation of myosin II (MII) filament composition allows tuning of surface tension at the cortex to maintain cell shape during cytokinesis. Our results reveal that MIIA generates cortex tension, while MIIB acts as a stabilizing motor and its inclusion in MII hetero-filaments reduces cortex tension. Tension generation by MIIA drives faster cleavage furrow ingression and bleb formation. We also show distinct roles for the motor and tail domains of MIIB in maintaining cytokinetic fidelity. Maintenance of cortical stability by the motor domain of MIIB safeguards against shape instability-induced chromosome missegregation, while its tail domain mediates cortical localization at the terminal stages of cytokinesis to mediate cell abscission. Because most non-muscle contractile systems are cortical, this tuning mechanism will likely be applicable to numerous processes driven by myosin-II contractility.

In Brief—Taneja et al. describe distinct roles for the two myosin-II paralogs in regulating actin cortex mechanics during cell division. Myosin-IIA generates cortex tension, while myosin-IIB maintains cortical stability. Optimal levels of the two paralogs within hetero-filaments at the cortex are required for shape stability and cytokinetic fidelity during cell division.

Graphical abstract

*Correspondence: dylan.burnette@vanderbilt.edu.

AUTHOR CONTRIBUTIONS

D.T.B. and N.T. designed experiments. N.T., S.M.B., and A.M.F. performed experiments. N.T., M.R.B., A.M.F., and J.A.C. analyzed the data. M.R.B. and W.D.M. helped in the interpretation of cell indentation experiments. R.O. helped in experiment design. V.G. provided access to reagents (human H9 ESC cell line). N.T. and D.T.B. wrote the manuscript. All authors read and commented on the manuscript.

SUPPLEMENTAL INFORMATION

Supplemental Information can be found online at https://doi.org/10.1016/j.celrep.2020.03.041.

DECLARATION OF INTERESTS

The authors declare no competing interests.

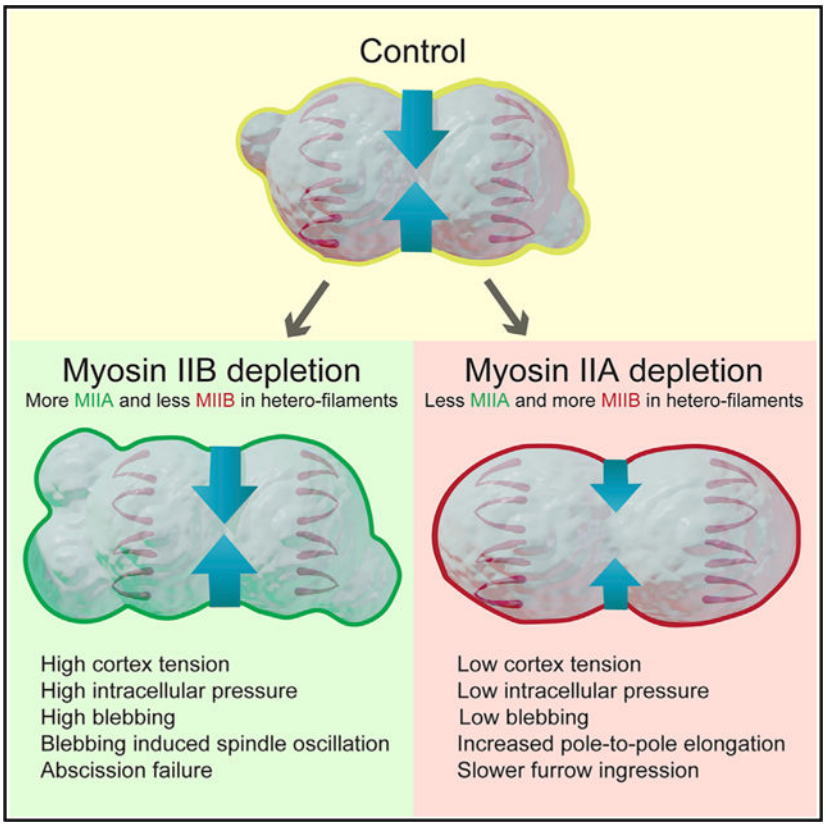

INTRODUCTION

The cortex of animal cells is a thin network of actin filaments underneath the plasma membrane. The cortex provides mechanical support to the membrane and organizes protein complexes (Fritzsche et al., 2016; Salbreux et al., 2012; Sezgin et al., 2017). Membrane and actin cross-linkers, in addition to the molecular motor myosin II (MII), organize and remodel this dynamic structure. Through the modulation of its mechanical properties, the cortex allows cells to change shape and generate tension in response to internal and external stimuli. In the case of migratory responses, such as those observed during development and disease progression, the cortex can remodel to produce protrusions such as filopodia, lamellipodia, and blebs (Charras and Paluch, 2008; Gardel et al., 2010). During mitosis, the cortex undergoes a series of remodeling events, where it initially allows a cell to round up, and then finally divide into two through the constriction of an equatorial contractile ring (Maddox and Burridge, 2003; Stewart et al., 2011; Surcel et al., 2010).

The cytokinetic phase of cell division presents a major challenge to cortical stability due to the extensive remodeling events required at the cleavage furrow. During cytokinesis, a transient enrichment of MII and actin at the equatorial cortex creates a contractile network that contains highly organized actomyosin ensembles called “stacks” (Fenix et al., 2016; Fishkind and Wang, 1993; Fujiwara and Pollard, 1976). While both commonly expressed paralogs of MII, MIIA and MIIB, co-assemble in the cleavage furrow (Beach et al., 2014), functional differences in driving ingression have begun to be elucidated. It was recently

reported that knockout (KO) of MIIA, but not MIIB, leads to slower ingression at the equatorial cortex (Yamamoto et al., 2019). The authors found this correlated with larger MII stacks at the equatorial cortex, calling into question whether formation of stacks is required for force generation at the equatorial cortex, or is inhibitory to furrow ingression (Yamamoto et al., 2019).

While multiple studies have heavily focused on mechanisms driving contractile ring formation and ingression, relatively fewer studies have focused on the polar actomyosin network. At the polar region of dividing cells, the cortex retains the same isotropic organization found in rounded metaphase cells and contains lower MII activity (Bovellan et al., 2014; Levayer and Lecuit, 2012). Accumulation of MII at the cortex creates cortical tension; that, in turn, increases intracellular pressure (Stewart et al., 2011). Excess intracellular pressure is released at the polar cortex by formation and growth of membrane protrusions called “blebs” (Sedzinski et al., 2011). It was recently reported that KO of MIIA, but not MIIB, results in reduced polar blebs during cytokinesis and reduced cortex stiffness during metaphase (Yamamoto et al., 2019). The mechanism underlying reduced polar bleb formation upon MIIA KO remains unclear, since contributions of MIIA and MIIB to cortex tension and intracellular pressure remain unknown.

Perturbation of the polar cortical network can result in shape instability and cytokinetic failure (Guha et al., 2005; Sedzinski et al., 2011). For instance, knockdown of anillin, an actin binding scaffold protein, results in a global increase in cortical instability due to enhanced cortical contractility (Sedzinski et al., 2011; Straight et al., 2005). Reducing polar contractility at one pole through local delivery of blebbistatin, an inhibitor of the ATPase activity of MII, results in cytokinetic failure and misplaced cleavage furrows (Guha et al., 2005). This has resulted in the general idea that the cortex of dividing cells is inherently prone to shape instabilities, and cortical contractility therefore must be tightly regulated.

In this study, we investigate the role of MIIA and MIIB in regulating actin cortex mechanics at the equatorial and polar cortex. In contrast with a previous report (Yamamoto et al., 2019), we show that MIIA depletion reduces MII stacks at the cleavage furrow. At the polar cortex, depletion of one paralog leads to compensatory localization of the other, resulting in changes in MIIA/B hetero-filament composition. We further show cortex tension is tuned as a result of these changes in filament composition, with higher MIIA in hetero-filaments correlating with higher cortex tension and intracellular pressure. Perturbation of this tuning results in cell shape instabilities and chromosome missegregation. These findings also uncover a general mechanism that may allow cells to attain a broad range of contractile states in order to perform various cellular functions requiring cortex contractility.

RESULTS

MIIA Templates MII Filament Ensembles at the Equatorial Cortex to Drive Ingression

We first investigated the role of the predominant MII paralogs— MIIA and MIIB—in the two cortical networks during cytokinesis. HeLa cells express MIIA and MIIB, but not MIIC (Taneja and Burnette, 2019). MIIA and MIIB filaments are known to co-assemble in the same filament in the cleavage furrow (Beach et al., 2014). MIIA is required to template

MIIB filament stacks at the leading edge of migrating cells during interphase (Fenix et al., 2016). It was recently reported that KO of MIIA results in larger MIIB stacks in fibroblasts (Yamamoto et al., 2019), suggesting the templating of MII stacks by MIIA does not occur during cytokinesis. To test whether a similar effect occurs in HeLa cells, we depleted MIIA using siRNA ($MIIA^{lo}$ cells, Figures S1A–S1D). We observed a nearly 50% compensatory increase in total MIIB protein levels in $MIIA^{lo}$ cells (Figure S1A).

We used a method we previously developed to measure the length of MII filament stacks using structured illumination microscopy (SIM) (Fenix et al., 2016). Intriguingly, depletion of MIIA significantly reduced the length of MIIB stacks at the cleavage furrow (Figures 1A and 1C, $p = 0.004$). Protein level compensation by MIIA upon MIIB depletion ($MIIB^{lo}$ cells) was more modest (20%, Figure S1A). Consistent with the templating hypothesis, we found no change in MIIA stacks in the cleavage furrow of $MIIB^{lo}$ cells (Figures 1B and 1C). To test whether the differences between our results and a previous report were a result of knockdown in HeLa cells versus KO in fibroblasts, we also measured stack lengths in MIIA-KO HAP1 fibroblasts (Taneja and Burnette, 2019). We found KO of MIIA also resulted in smaller MIIB stacks (Figure S2A).

It was recently proposed that MII stacking is inhibitory to cleavage furrow ingression, with larger MII stacks upon MIIA KO resulting in slower ingression (Yamamoto et al., 2019). Therefore, we hypothesized smaller stacks in $MIIA^{lo}$ cells should result in faster cleavage furrow ingression. Surprisingly, MIIA depletion caused a 1.4-fold reduction in cleavage furrow ingression rates compared to scrambled control siRNA (Scr) or $MIIB^{lo}$ cells (Figures 1D and 1E, $p = 0.0006$ for Scr versus $MIIA^{lo}$). To rule out off-target effects of siRNA knockdown of MIIA, we rescued MIIA depletion using full-length, siRNA-resistant MIIA-mEGFP. Expression of MIIA-mEGFP at 65% of endogenous MIIA levels increased ingression to control rates (Figure 1F; Table S1). Importantly, overexpression of MIIB at 143% of endogenous MIIB levels did not increase rate of cleavage furrow ingression in $MIIA^{lo}$ cells (Figure 1G; Table S1). This suggested that while the requirement for MIIA in driving faster cleavage furrow ingression was consistent with recent reports (Yamamoto et al., 2019), MII stacking was not inhibitory to furrow ingression.

To test whether MIIA is sufficient to increase furrow ingression rates, we used HAP1 fibroblasts. We first depleted >99% of MIIB using siRNA (Figure 1I, inset). Knockdown of MIIB in HAP1 parental cells did not result in change in ingression rates, similar to HeLa cells. On the other hand, CRISPR-mediated KO of MIIA resulted in a 1.4-fold reduction in cleavage furrow ingression rates (Figure 1H and 1I, $p < 0.0001$ for Parental versus MIIA KO). Expression of MIIA-mEGFP, but not MIIB-mEGFP, increased cleavage furrow ingression rates in HAP1 MIIA KO fibroblasts (Figures 1H and 1I). Interestingly, we also found that the amount of MIIA localized to the equatorial cortex positively correlated with ingression rates in human embryonic stem cell (hESC) colonies—which show a natural gradient of MIIA, but not MIIB levels, within the colony (Figure S2). Taken together, these data show that MIIA, but not MIIB, is necessary and sufficient to drive faster ingression through templating of MII stacks at the cleavage furrow.

Loss of MIIB Results in Shape Instabilities at the Polar Cortex

Despite no change in furrow ingression in MIIB^{lo} cells, we noted using high-resolution differential interference contrast (DIC) imaging that MIIB^{lo} cells showed dramatic shape instabilities during cytokinesis in the form of large membrane blebs (4.2-fold higher total bleb surface area per min, $p < 0.0001$) (Figures 2A– 2C; Video S1). This result was surprising, since no change in polar blebbing was reported upon KO of MIIB in fibroblasts (Yamamoto et al., 2019). On the other hand, consistent with the previous report (Yamamoto et al., 2019), MIIA^{lo} cells showed reduced blebbing compared to Scr cells (3-fold lower total bleb surface area per min, $p = 0.0096$) (Figures 2A–2C). The blebbing events in MIIB^{lo} cells were associated with spindle rocking behavior (Video S1), as has been observed previously upon destabilization of the polar cortex at one pole or depletion of moesin (Carreno et al., 2008; Sedzinski et al., 2011). Expression of siRNA resistant MIIB-mEGFP at 119% of endogenous levels significantly reduced blebbing events in MIIB^{lo} cells (Figures 2A and 2B; Table S1). Overexpression of MIIA at 116% of endogenous levels in MIIB^{lo} cells did not reduce blebbing events (Figures 2A and 2B; Video S2). Conversely, expression of siRNA resistant MIIA-mEGFP in MIIA^{lo} cells rescued blebbing, while overexpression of MIIB-mEGFP in MIIA^{lo} cells did not increase blebbing (Figure 2C; Video S2). These data show that the increase and decrease in blebbing were specific to MIIB and MIIA depletion, respectively.

To test if loss of MIIA is associated with reduced blebbing during interphase, we turned to filamin-deficient M2 melanoma cells. M2 cells are a classical model for blebbing, since a large proportion of these cells constitutively blebs (Bovellan et al., 2014; Charras et al., 2006; Cunningham, 1995). We found 50% of Scr M2 cells blebbed. Knockdown of MIIA, but not MIIB, reduced the proportion of blebbing M2 cells (Figures 2D–2F and S3A). Expression of MIIA-mEGFP in MIIA^{lo} M2 cells increased the proportion of blebbing cells (Figure 2F). These data therefore suggest loss of MIIA is correlated with less frequent blebbing, while loss of MIIB is correlated with more frequent blebbing.

The shape instabilities observed in MIIB^{lo} cells led us to further analyze cell shape upon depletion of the two paralogs. Specifically, we noted that MIIA^{lo} cells tended to elongate more than Scr cells during cytokinesis (Figure 2G). We quantified this cell shape alteration by measuring the increase in pole-to-pole distance during cytokinesis relative to metaphase (Figure 2H). Indeed, MIIA^{lo} cells showed a 13% longer pole-to-pole distance compared to Scr or MIIB^{lo} cells (Figure 2I, $p = 0.013$ for Scr versus MIIA^{lo}). Expression of MIIA in MIIA^{lo} cells significantly reduced pole-to-pole elongation (Figure S3B). On the other hand, overexpression of MIIB in MIIA^{lo} cells did not rescue this defect (Figure S3B; Video S2). Taken together, our results show that depletion of either paralog leads to distinct alterations to cell shape during cytokinesis.

Depletion of MII Paralogs Leads to Changes in MII Localization and Hetero-Filament Composition

MIIA and MIIB co-localize during metaphase and ingression (Yamamoto et al., 2019). We confirmed this by both co-expressing MIIA mApple and MIIB mEmerald in HeLa cells, as well as endogenous labeling (Figures S4A and S4B; Video S3). We found that MIIB was

cortically enriched as early as metaphase, whereas MIIA was only weakly enriched at the metaphase cortex (Figure S4A). After completion of furrow ingression (i.e., late cytokinesis), MIIA enrichment at the cortex was lost, while MIIB remained distinctly enriched at the equatorial cortex (Figure S4A; Video S3). Since there were only subtle differences in MIIA and MIIB localization, other mechanisms must therefore account for the differences in phenotypes observed upon knockdown of MII paralogs; that is, the phenotypes observed are not due to only one paralog localizing to the polar cortex.

We hypothesized that depletion of one paralog could lead to a change in the localization of the other. To test this, we localized endogenous MIIA and MIIB in Scr versus MIIB^{lo} and MIIA^{lo} cells, respectively. At the equatorial cortex, we noted only MIIB compensated for MIIA upon MIIA depletion (Figure S4C). On the other hand, depletion of either paralog led to a compensatory increase in localization of the other at the polar cortex (Figures 3A–3C). We observed this compensatory behavior even at the metaphase cortex (Figures 3D and 3E). Expression of MIIA in MIIA^{lo} cells at 60% of endogenous levels reduced MIIB localization at the cortex (Figure S4D; Table S1). Similarly, expression of MIIB in MIIB^{lo} cells at 123% of endogenous levels reduced MIIA localization at the cortex (Figure S5E). Taken together, our data show that knockdown of either paralog leads to a change in the relative abundance of the two paralogs at the cortex.

We next wanted to investigate the molecular basis for the compensatory localization of MII paralogs at the polar cortex. While hetero-filaments of MIIA and MIIB have been reported at the cleavage furrow using SIM (Beach et al., 2014) the composition of MII filaments at the polar cortex has remained unexplored. To that end, we performed SIM of endogenous MIIA and MIIB at the polar cortex. We found that 96% of MIIB filaments co-localized with MIIA in control cells, while 58% of MIIA filaments contained MIIB (Figures 3F and 3G). Depletion of MIIA resulted in a significant decrease in MIIA intensity at the cortex, accompanied by a significant increase in the proportion of the residual MIIA filaments containing MIIB (91%, $p < 0.0001$) (Figures 3F–3H). Interestingly, the proportion of MIIB filaments containing MIIA remained unchanged. Conversely, depletion of MIIB resulted in a significant decrease in the proportion of MIIA filaments containing MIIB, with only 15% of MIIA filaments positive for MIIB (Figures 3F–3H, $p < 0.0001$). We again found that ~99% of the residual MIIB was in hetero-filaments with MIIA. Taken together, our results show that knockdown of MIIA results in an increase in the proportion of MIIB-containing hetero-filaments while knockdown of MIIB results in a decrease in the proportion of MIIB-containing hetero-filaments. We next wanted to investigate how these changes in filament composition alter the biophysical properties of the cortex.

Depletion of MIIA Results in Reduced Cortex Tension and Intracellular Pressure

A recent study reported that MIIA, but not MIIB, KO results in reduced cortex stiffness, which the authors proposed underlies reduction in blebbing (Yamamoto et al., 2019). This is contrary to the well-established concept that cortex tension, not stiffness, is the direct result of actomyosin contractility and thus drives initiation and growth of blebs (Paluch et al., 2005; Tinevez et al., 2009). We therefore investigated how changes in MII filament composition altered cortex tension and stiffness. Micropipette aspiration can be used to

measure cortex tension as well as elastic properties of cells to measure stiffness (Brugués et al., 2010; Kee and Robinson, 2013; Tinevez et al., 2009). We chose to perform these measurements during metaphase, since (1) we found compensation in localization during metaphase; (2) the metaphase cortex is uniform and devoid of the fluctuations in MII localization that occur at the polar cortex (Video S3); and (3) polar cortex blebbing would interfere in cortex tension measurements. Consistent with previous reports, we found knockdown of MIIA resulted in reduced cortex stiffness (Figure S5A) (Yamamoto et al., 2019). Since MIIB^{lo} cells show a higher degree of blebbing, we expect MIIB^{lo} cells to be stiffer. However, we found stiffness was unaltered in MIIB^{lo} cells (Figure S5A), as also previously reported for MIIB KO (Yamamoto et al., 2019). These data suggest that changes in stiffness are not sufficient to explain the observed differences in bleb initiation, since stiffness in MIIB^{lo} cells is unaltered despite dramatic increases in blebbing.

We then measured cortex tension using micropipette aspiration and found a significant reduction (~4-fold) in cortex tension in MIIA^{lo} versus Scr cells (Figure 4A, $p < 0.0001$). Expression of MIIA-mEGFP at 72% of endogenous levels increased cortex tension to approximately control levels (Figure 4B). As an additional control for these measurements, we treated Scr cells with 50-μM blebbistatin, and measured cortex tension. As previously reported, blebbistatin significantly reduced cortex tension (Tinevez et al., 2009) (Figure 4B).

Conversely, we predicted that MIIB depletion should result in higher cortex tension as MIIB^{lo} cells show more blebbing. MIIB^{lo} cells had ~1.9-fold higher cortex tension compared to Scr cells (Figure 4B, $p = 0.0082$). Expression of MIIB-mEGFP at 197% of endogenous levels in MIIB^{lo} cells resulted in a decrease in cortex tension comparable to control levels (Figure 4B). Taken together, our results show MIIA depletion results in lower cortex tension, while MIIB depletion results in higher cortex tension, which correlated with the observed frequencies of bleb initiation we observed during cytokinesis (Figure 2). Despite increased cortex tension in MIIB^{lo} cells, these cells did not bleb during metaphase. To test if increasing pressure could induce blebbing, we compressed MIIB^{lo} cells in metaphase with a microneedle. We observed MIIB^{lo} cells blebbed 80% of the time upon indentation, while Scr and MIIA^{lo} cells showed negligible blebbing (Figures S5B and S5C; Video S4).

We next wanted to directly interrogate the relative contributions of MIIA and MIIB to bleb growth. It has been previously reported that MII-driven cortex tension promotes bleb growth by creating hydrostatic pressure (Tinevez et al., 2009). Blebs created by disruption of the cortex using localized laser ablation are thought to mimic the initiation of spontaneous blebs (Goudarzi et al., 2012; Tinevez et al., 2009). The size of the bleb created immediately following ablation is positively correlated with the instantaneous intracellular pressure. Ablation of the metaphase cortex of Scr cells resulted in the creation of a bleb, which subsequently retracted over a period of 45–90 s, as has been reported previously (Figure 4C) (Charras et al., 2006; Taneja and Burnette, 2019). Since MIIA^{lo} cells have lower cortex tension, we hypothesized that smaller blebs would be created in these cells. To test this, we created blebs using laser ablation at the metaphase cortex of MIIA^{lo} cells and measured the size of the bleb immediately following ablation (Figure 4C). Small or no blebs were created immediately following ablation in MIIA^{lo} cells (Figures 4C and 4D, $p < 0.0001$ for Scr

versus MIIA^{lo}). Interestingly, these blebs failed to retract and instead exhibited a period of slow growth over extended time periods of up to 4 min (Figures 4C and S6). Expression of MIIA-mEGFP increased bleb size comparable to Scr cells, as well as restored bleb retraction (Figure 4D). This role of MIIA in driving bleb retraction was consistent with our previous report (Taneja and Burnette, 2019).

Conversely, we hypothesized larger blebs should be created upon depletion of MIIB due to increased cortex tension. We found 1.6-fold larger blebs were created in MIIB^{lo} cells upon laser ablation, and these blebs all successfully retracted (Figures 4C, 4D, and S6; $p = 0.0020$ for Scr versus MIIB^{lo}). To test whether the pressure driving bleb growth was specifically generated by MII driven cortex tension, we performed ablation in cells treated with 50-μM blebbistatin. Indeed, blebbistatin treatment mimicked MIIA depletion, with small or no blebs created upon ablation, and exhibited slow bleb growth instead of retraction (Figures 4C, 4D, and S6). Taken together, our results show MIIA-driven cortex tension creates larger blebs upon ablation during metaphase.

We next proceeded to test whether MIIA drives growth of larger blebs at the polar cortex during cytokinesis. To that end, we performed laser ablation of the polar cortex during cytokinesis in Scr versus MIIA^{lo} and MIIB^{lo} cells (Figure 4E). We observed that blebs created at the polar cortex of Scr cells resulted in blebs that were, on average, larger than those created during metaphase (Figure 4F, compared to Figure 4D), consistent with the idea that intracellular pressure increases following anaphase onset (Stewart et al., 2011). Depletion of MIIA resulted in the creation of smaller blebs that failed to retract, while MIIB depletion resulted in larger blebs compared to Scr cells (Figures 4E and 4F).

We then wanted to test whether MIIA is sufficient to drive bleb growth. To that end, we performed laser ablation of the polar cortex of HAP1 fibroblasts. We observed that very small or no blebs were created in MIIA KO cells compared to control parental cells or MIIB^{lo} parental cells (Figures 4G and S5D). Expression of MIIA, but not MIIB, resulted in restoration of bleb formation upon ablation (Figures 4G and S5D). To further test if MIIA is sufficient to drive higher bleb growth, we turned to Cos7 cells, which do not express MIIA. Indeed, expression of MIIA, but not MIIB, increased bleb size upon ablation of the polar cortex during cytokinesis (Figure S5E). Taken together, our results show that MIIA is both necessary and sufficient to drive the growth of larger blebs.

MII Motor Domains Dictate the Relative Contribution of MII Paralogs

Previous studies have shown that the C terminus of MII regulates paralog localization (Sandquist and Means, 2008; Vicente-Manzanares et al., 2008). The observed similarities in localization dynamics of MIIA and MIIB at the polar cortex (Figure S4) suggest that the N-terminal motor domains might account for the distinct roles played by the two paralogs during cytokinesis. Most characterizations of MII motor activity *in vitro* has been performed using N-terminal S1 fragments (Kovács et al., 2003; Rosenfeld et al., 2003; Wang et al., 2003). Therefore, a chimeric MII, bearing the motor domain of MIIB, and the coiled-coil domain and tail piece of MIIA (MIIB/A), should be able to rescue blebbing in MIIB^{lo} cells by competing with endogenous MIIA motors at the polar cortex, independent of the tail domain. As expected, this chimeric motor showed a localization pattern similar to MIIA,

with weaker cortical enrichment (Figure 5A), consistent with previous findings that the tail of MIIB determines its subcellular localization (Sandquist and Means, 2008; Vicente-Manzanares et al., 2008). Strikingly, expression of the MIIB/A chimera at levels comparable to full-length MIIB (Table S1) resulted in significant suppression of blebbing (Figure 5B).

Conversely, MIIB is upregulated at the polar cortex in MIIA^{lo} cells (Figures 3A–3C); therefore, we hypothesized that increasing MIIA motors in the polar cortex should increase blebbing in MIIA^{lo} cells. To test this, we expressed a chimera bearing the motor domain of MIIA and the coiled-coil domain and tailpiece of MIIB (MIIA/B) in MIIA^{lo} cells. This construct also faithfully mimicked MIIB localization, showing a clear cortical enrichment, as well as distinct equatorial localization during late cytokinesis (Figure 5A). Interestingly, we observed a significant increase in blebbing upon expression of MIIA/B at levels comparable to full-length MIIA (Table S1; Figure 5C). Furthermore, this construct also significantly increased cleavage furrow ingression rates in MIIA^{lo} cells (Figure 5D). Increased pole-to-pole elongation observed in MIIA^{lo} cells was also rescued by the MIIA/B chimera (Figure 5E). To test whether suppression of the MIIA and MIIB depletion phenotypes correlated with changes in cortex tension, we performed micropipette aspiration on MIIA^{lo} expressing MIIA/B-mEGFP and MIIB^{lo} cells expressing MIIB/A-mEGFP. In line with our observations for ingression, blebbing, and pole-to-pole elongation, we found MIIB/A expression in MIIB^{lo} cells significantly decreased cortex tension, while MIIA/B expression in MIIA^{lo} cells significantly increased cortex tension (Figure 5F). To test whether these changes in cortex tension resulted in increased bleb growth, we expressed MIIA/B mEGFP and MIIB/A mEGFP in HAP1 MIIA-KO cells and performed cortex ablation during cytokinesis. Expression of MIIA/B, but not MIIB/A significantly increased initial bleb size following ablation (Figure 5G). Taken together, these data suggest that the motor domain determines the paralog-specific contribution of the two paralogs at the polar and equatorial cortex.

MIIB Depletion Results in Cytokinetic Failure

We finally wanted to assess the effects of MII paralog depletion upon cytokinetic fidelity. To that end, we measured the proportion of binucleated cells as a proxy for failed cytokinesis. We found that MIIA loss resulted in a mild increase in binucleated cells (Figures 6A and 6B). As an intended control, we measured binucleation in MIIB^{lo} HeLa cells. Surprisingly, we observed a dramatic, nearly 10-fold, increase in binucleated MIIB^{lo} cells relative to Scr cells (Figures 6A and 6B). Expression of siRNA-resistant MIIB resulted in a significant decrease in binucleation (Figure 6C). To test which domain(s) of MIIB was sufficient to rescue the binucleation defect, we expressed the MIIB/A and MIIA/B chimeras in MIIB^{lo} cells. Interestingly, both chimeras partially rescued the binucleation defect (Figure 6C).This prompted us to investigate the contribution of the two domains to cytokinetic fidelity.

We noted that a subset of binucleated cells were adjacent to an enucleated cell (cytoplast) (Figure 6D). We wondered whether dramatic spindle oscillation observed during blebbing in MIIB^{lo} cells could lead to this phenotype, where one daughter cell may inherit both sets of chromosomes. Since the MIIB/A chimera suppressed blebbing (Figure 5), while the MIIA/B chimera increased blebbing, we hypothesized that expression of these chimeras should alter the proportion of this oscillation-induced binucleation. We first introduced full-length MIIB

or MIIB/A in MIIB^{lo} cells, both of which suppress blebbing. Expression of both constructs led to a significant decrease in the proportion of cells that were binucleated and adjacent to an enucleated cell (Figure 6E). Expression of the MIIA/B chimera, which increases blebbing, resulted in a significant increase in the proportion of cells that were binucleated and adjacent to an enucleated cell (Figure 6E). These data suggested that blebbing positively correlates with increased incidence of oscillation-induced chromosome missegregation.

It was previously theorized that the retraction of large blebs creates large changes in intracellular pressure (Sedzinski et al., 2011). To test whether spindle oscillation was correlated with the retraction of large blebs, we performed closer analysis of oscillation events in MIIB-depleted cells. Indeed, spindle displacement was correlated with the retraction of large blebs (Figures 7A and 7B). Furthermore, the extent of displacement positively correlated with the size of the bleb (Figure 7B). We therefore predicted that cells with higher mean bleb size should show spindle oscillation, rather than cells with higher number of blebs. Indeed, we found that cells showing spindle oscillation had a significantly higher mean bleb size compared to non-oscillating cells (Figure 7C). These results show that creation of large blebs increases the probability of spindle oscillation, which could drive chromosome missegregation.

We next wanted to directly visualize oscillation-induced chromosome missegregation in live cells. To that end, we visualized chromosomes using H2B-mCherry and performed live imaging of MIIB^{lo} cells undergoing cytokinesis. Strikingly, we observed that dramatic spindle oscillation in MIIB^{lo} cells did result in one daughter cell inheriting both sets of chromosomes and becoming binucleated, while the other daughter cell was enucleated (Figure 7D; Video S5). Furthermore, while the initiation of spindle oscillation correlated with the initiation of polar blebs, subsequent oscillations were accompanied by cortical contractions of entire daughter cells (Video S5). We found 20.0% of all binucleation events resulted from an oscillation-dependent mechanism (Figures 7F and S7A). Interestingly, 42.5% of all binucleation events instead resulted from abscission failure in the absence of spindle oscillations, resulting in one binucleated cell (Figures 7E, 7F, and S7B). The remaining 37.5% of binucleation events were accompanied by both spindle oscillation and abscission failure, resulting in one binucleated cell (Figure S7C).

To investigate the mechanism for these distinct modes of binucleation, we introduced MII chimeras and measured the relative incidence of oscillation-induced chromosome missegregation and abscission failure. The MIIB/A chimera suppresses blebbing, and therefore should suppress oscillation-induced chromosome missegregation. Indeed, expression of MIIB/A in MIIB^{lo} cells reduced the proportion of oscillation-induced chromosome missegregation, accompanied by an increase in the proportion of cells that underwent abscission failure (Figure 7F). It was recently proposed that MIIB could play a role in stabilizing the intracellular bridge to facilitate abscission (Wang et al., 2019). In support of this hypothesis, MIIB showed an enrichment at the equatorial cortex at the end of cytokinesis (Figure S4A, yellow arrow). Consistent with the tail domain regulating localization, the MIIB/A chimera did not show the late equatorial enrichment at the cortex (Figure 5A). Taken together, these data suggest that oscillation-induced binucleation is suppressed by the ability of the motor domain of MIIB to regulate blebbing.

As opposed to the MIIB/A chimera, the MIIA/B chimera increases blebbing, but still shows enrichment at the equatorial cortex at the end of cytokinesis (Figure 5A, white arrow). Therefore, this construct should not suppress oscillation-induced chromosome missegregation. Indeed, we observed an increase in the proportion of oscillation-induced binucleation (Figure 7F). Conversely, the proportion of binucleation events accompanied by abscission failure was reduced (Figure 7F). These data suggest that the tail domain regulates MIIB's ability to facilitate abscission, possibly by driving the late enrichment of MIIB at the equatorial cortex.

DISCUSSION

The majority of non-muscle contractile systems observed in animal cells are cortical and modulation of these contractile systems can drive diverse processes during development and disease progression (Levayer and Lecuit, 2012; Salbreux et al., 2012). During cytokinesis, the cortex is organized into two distinct networks: equatorial and polar. We show MIIA and MIIB both localize to the equatorial network in the form of MII filament stacks. Our data reveal that MIIA is required for templating MII filament stacks. In line with this templating activity, MIIA was necessary and sufficient to drive faster cleavage furrow ingression. Interestingly, a recent study also found a requirement for MIIA in driving ingression (Yamamoto et al., 2019). However, they claimed that CRISPR KO of MIIA results in larger MIIB stacks at the cleavage furrow, and that MII stacking is somehow inhibitory to furrow ingression. A requirement for MIIA in templating MIIB stacks at the leading edge during interphase has been well documented by our group and others (Fenix et al., 2016; Shutova et al., 2014). We therefore find it unlikely that MIIA is not required for templating MII stacks at the cleavage furrow. Our data suggest that organization of MII filaments into stacks is required for faster ingression, consistent with multiple theoretical studies that suggest increased order within cytoskeletal assemblies is associated with higher force generation (Dasbiswas et al., 2019; Friedrich et al., 2011; Zemel et al., 2010).

Our results also shed new light on the mechanics of the polar cortex. During cytokinesis, the polar cortex is characterized by blebbing, which is thought to serve as a mechanism of intracellular pressure release (Sedzinski et al., 2011). Theoretical studies have suggested that blebs are initiated due to surface tension that drives cortex rupture or detachment (Paluch et al., 2005). We found knockdown of MIIA and MIIB had opposing phenotypes on blebbing, with MIIA depletion reducing bleb formation, and MIIB depletion increasing bleb formation. These changes in blebbing correlated with changes in cortex tension. Our results show that MIIA, but not MIIB, generates the majority of surface tension at the cortex. At the molecular level, we speculate this may be driven by increased buckling of actin filaments by MIIA (Murrell and Gardel, 2012).

A recent study reported that MIIA, but not MIIB, KO reduced cortex stiffness (Yamamoto et al., 2019). The study also reported a reduction in the proportion of blebbing cells upon MIIA KO (0/10 cells), and no changes upon MIIB KO (8/10 cells in MIIB KO versus 9/10 in control), concluding that changes in stiffness drive the frequencies of blebbing. We also found stiffness remained unchanged upon MIIB depletion (Figure S5A). However, blebbing significantly increased upon MIIB knockdown (Figure 2). This apparent discrepancy results

from the fact that Yamamoto et al. (2019) reported blebbing as a binary measurement, as opposed to the detailed quantification of the number and size of blebs performed in this study. Indeed, when simply measuring the frequency of blebbing cells, the increase upon MIIB depletion was not dramatic (14/18 control cells versus 15/15 MIIB^{lo} cells). Furthermore, it is important to note that cortex stiffness is dependent on both the cortex tension (determined by MII contracting actin filaments), and the viscoelastic response of the cortex (determined by actin architecture) (Heer and Martin, 2017; Levayer and Lecuit, 2012; Salbreux et al., 2012). While the role of MII in cortex stiffness is an interesting question, it does not directly pertain to bleb initiation. Indeed, previous work has demonstrated that MII contractility can both stiffen and soften actin gels, depending on ATP levels, suggesting the effects of MII contractility on cell stiffness will be context dependent (Gardel et al., 2008). Taken together, our results show that MIIA generates cortex tension, which drives the initiation of polar blebs during cytokinesis.

Careful measurement of blebbing in MIIB^{lo} cells led us to perform a quantitative analysis of MIIA and MIIB localization at the polar cortex. We found the increase in cortex tension and blebbing upon MIIB depletion was driven by an increase in MIIA localization at the cortex. A similar compensatory localization by MIIB was observed upon MIIA depletion. These data reveal a mechanism to tune cortex tension by altering the relative levels of MIIA and MIIB at the cortex. There are multiple possible mechanisms for achieving this tuning at the molecular level. One possible mechanism is that the two paralogs compete for cortical occupancy; the other mechanism is through modulation of filament composition of MIIA/MIIB hetero-filaments. Super-resolution imaging of MIIA and MIIB at the cortex suggests support for the latter mechanism. MIIB showed a high propensity to associate with MIIA filaments, since the majority of MIIB co-localized with residual MIIA at the cortex upon MIIA knockdown. This argues against direct competition between the two paralogs, since cortical binding sites were in excess in comparison to the motors. Instead, we found the proportion of MIIA filaments that contained MIIB was altered in the knockdown conditions. Taken together, our results suggest tuning of cortex tension is achieved through the addition of MIIB to MIIA/MIIB hetero-filaments, rather than by seeding new filaments. Indeed, adding as little as 6 MIIB hexamers to 24 MIIA hexamers was sufficient to tune the properties of the filament to allow processive walking along an actin filament *in vitro* (Melli et al., 2018). This ratio of ~4:1 (MIIA:MIIB) is thus sufficient to change the biophysical properties of the filament *in vitro*.

On face value, this mechanism seems unlikely to work in cells as proteomic analysis has demonstrated that there is vastly more MIIA in HeLa cells than MIIB. The HeLa subtype (CCL-2) used in this study contains 93.5% MIIA and 6.5% MIIB, with no MIIC detected (Bekker-Jensen et al., 2017), yielding a ratio of ~14:1 (MIIA:MIIB). This leads to the question: how could tuning be accomplished with such an apparent abundance of MIIA?

A higher level of MIIB assembles into filaments compared to MIIA *in vitro* at similar concentrations and salt conditions (Murakami et al., 1995; Nakasawa et al., 2005). It was also reported that ~30% of total MIIB, and only ~8% of total MIIA, assembled into filaments in HeLa cells, using the amount of MII that was in the supernatant (i.e., soluble) and cytoskeletal (i.e., insoluble) fractions (Schiffhauer et al., 2019; Surcell et al., 2019). This

group also used the CCL-2 subtype. By combining the total amount of MIIA and MIIB from proteomics with the fraction of MIIA and MIIB within filaments, we calculated a 4:1 ratio MIIA:MIIB assembled in filaments (Table S2), in agreement with the ratio of MIIA:MIIB to change the properties of a hetero-filament *in vitro*.

We also showed that loss of MIIA, but not MIIB, resulted in lower ingression rates and bleb growth upon ablation in HAP1 fibroblasts. HAP1 cells contain a ratio of 2.4:1 of total MIIA:MIIB measured using proteomics (Jonckheere et al., 2018). We found that 24% ± 3% of MIIA and 40% ± 9% of MIIB was in the cytoskeletal fraction (Figure S8A). This yields an effective ratio of 1.5:1 of MIIA:MIIB assembled into filaments in control HAP1 cells (Table S2). These data argue against the possibility that the paralog-specific roles we observed for MIIA and MIIB are due to biased expression levels of the two paralogs.

Alternatively, the two paralogs could be functionally equivalent, and contractility is simply a function of the total amount of myosin II in the cell. For instance, the lack of rescue in ingression rates observed upon MIIB overexpression in $MIIA^{lo}$ cells could be due to insufficient levels of total myosin II (Figure S8B). To test this hypothesis, we compared ingression rates of $MIIA^{lo}$ cells expressing low levels of MIIA versus high levels of MIIB, such that the total amount of myosin II was equal. Consistent with MIIA uniquely driving faster ingression, $MIIA^{lo}$ cells expressing even low levels of MIIA showed significantly higher ingression rates (Figures S8C and S8D).

Our data also shows that the motor domain of each MII paralog determines its contribution to cortex tension, with lower duty ratios and higher ATPase activity of MIIA associated with higher cortex tension. We were not surprised that MIIB did not play a larger role in generating cortex tension, since MIIB has a higher duty ratio than MIIA (Kovács et al., 2003; Rosenfeld et al., 2003; Wang et al., 2003). That is, MIIB binds actin in the force-generating state for a larger proportion of its mechanochemical cycle. Therefore, the canonical view of MIIB has been that it is adapted to maintain tension rather than generate tension, a view supported by previous experimental and theoretical studies (Melli et al., 2018; Milberg et al., 2017; Stam et al., 2015). Modeling studies on cortex tension generation have implicated MIIB as a cross linker at the cortex since it is a slower motor (Stam et al., 2015). Paralog-specific roles for MII have also been observed during regulated exocytosis *in vivo*, where MIIB was hypothesized to serve as a membrane stabilizer, while MIIA was hypothesized to generate tension to expand the fusion pore (Milberg et al., 2017). Here, we provide biophysical measurements in living cells to directly support these long-hypothesized views of MII paralogs in generating tension.

Interestingly, while the motor domain of MIIB was sufficient to tune cortex tension (Figure 5F), it only partially rescued MIIB's function in maintaining cytokinetic fidelity (Figure 6C). This line of inquiry revealed two non-mutually exclusive mechanisms of cytokinetic failure upon loss of MIIB. Loss of the motor function of MIIB, required to tune cortex tension, led to increased blebbing at the polar cortex. Retraction of large blebs led to oscillations of the mitotic spindle, resulting in both sets of chromosomes being pushed into one of the daughter cells, while the other daughter became enucleated. These data reveal a mechanism for chromosome missegregation through instabilities in cell shape. We also show that the tail

domain of MIIB contributes to abscission, independent of the specific biophysical properties of its motor domain, suggesting that the contribution of the motor or tail domain to MII function will be context dependent.

Our data implicating MIIB in mediating abscission supports previous suggestions that MIIB is important for the completion of abscission (Lordier et al., 2012). A recent study proposed that this function of MIIB in mediating abscission may be achieved through stabilizing the intracellular bridge (Wang et al., 2019). Of note, while the authors implicated MIIB during this process, knockdown of MIIB had no effect on binucleation. The authors proposed this was due to low knockdown efficiency of MIIB (60%). In our study, we achieved 80% knockdown of MIIB and did observe a significant increase in binucleation. Future studies will be required to reveal the precise mechanical mechanism of intracellular bridge stabilization.

Finally, it is interesting to note that organisms such as worms and flies contain only one MII paralog, leading to the question of how contractility is tuned in these organisms. One potential mechanism may be increased reliance on adhesion dependent cytokinesis. Indeed, organisms such as *Dictyostelium* and adhesive cell lines such as normal rat kidney (NRK) cells can divide without MII activity (Kanada et al., 2005; Neujahr et al., 1997). Another mechanism could involve regulating the amount of each paralog that can assemble into filaments, for instance through PKC activity (Schiffhauer et al., 2019). Finally, oscillations of upstream regulators of MII, which appear to be evolutionarily conserved from flies to mammals (Bement et al., 2015; Machacek et al., 2009; Martin et al., 2009), could regulate the level of MII activation. The mechanism we propose here adds an additional layer of control and tunability, likely acquired later in evolution, when MII paralogs diverged.

STAR★METHODS

LEAD CONTACT AND MATERIALS AVAILABILITY

Further information and requests for resources and reagents may be directed to and will be fulfilled by the Lead Contact, Dylan Burnette (dylan.burnette@vanderbilt.edu). All unique/stable reagents generated in this study are available from the Lead Contact without restriction.

EXPERIMENTAL MODEL AND SUBJECT DETAILS

Cell lines and growth conditions—HeLa (ATCC, CCL-2) and Cos7 cells (ATCC, CRL-1651) were cultured in growth media comprised of DMEM (Mediatech, Inc., Manassas, VA, #10-013-CV) containing 4.5 g/L L-glutamine, L-glucose, sodium pyruvate and supplemented with 10% fetal bovine serum (Sigma-Aldrich, St. Louis, MO, #F2442). HAP1 *myh9* (MIIA) KO and parental cells were purchased from Horizon discovery as previously described (Fenix et al., 2016), and cultured in IMDM medium supplemented with 10% fetal bovine serum. M2 melanoma cells were cultured in Minimal Essential Medium supplemented with Earle's salts, 10 mM HEPES and 10% fetal bovine serum. Growth substrates were prepared by coating #1.5 glass coverslips (*In vitro* Scientific,

#D35C4-20-1.5N or #D35-20-1.5N) with 10 μg/mL FN (Corning, Corning, NY, #354008) in PBS (Mediatech, Inc., #46-013-CM) at 37°C for 1 h.

Human embryonic stem cell lines H9 (WA09) were obtained from WiCell Research Institute (Madison, WI). Cells were seeded as undifferentiated colonies on plates coated with Matrigel (Corning, #354277), maintained at 37°C and 5% CO_2, and fed daily with mTeSR (Stem Cell Technologies #05850). Cells were passaged once they reached 80% confluency. For immunofluorescence, cells were plated on Matrigel-coated 35 mm glass bottom culture dishes (MatTek #P35G-0-140C) and experiments were performed the next day.

For protein expression, cells were transiently transfected using Fugene 6 (Promega, Madison, WI, #E2691) as per the manufacturer's instructions overnight in a 25-cm^2 cell culture flask (Genessee Scientific Corporation, San Diego, CA, #25-207) before plating on a growth substrate.

Alexa Fluor-488 phalloidin (#A12379), Alexa Fluor-568 phalloidin (#A12380) and Alexa Fluor 488-goat anti-rabbit (#A11034) were purchased from Life Technologies (Grand Island, NY). Rabbit anti-myosin IIA (#909801) was purchased from BioLegend (San Diego, CA). Rabbit anti-myosin IIB (#8824S and #3404S) was purchased from Cell Signaling Technology (Danvers, MA). The #8824S antibody was used in Figures S1A, S1C, S1D, S2C, 1A, 1C, S4B, and 3B–3E. The #3404S antibody was used in Figures S1B, S2A, S9A and S9B, S8A, 3F, S4D, and S4E.

Cell line authentication—The HeLa cell line used in this study was a gift of Dr. DA Weitz (Harvard University), and the M2 melanoma cells were a gift from Dr. Matthew Tyska. The Burnette lab had these lines authenticated by Promega and ATCC using their 'Cell Line Authentication Service' in 2015 and 2019, respectively. The methods and test results received from Promega and ATCC are as follows:

Methodology: Seventeen short tandem repeat (STR) loci plus the gender determining locus, Amelogenin, were amplified using the commercially available PowerPlex 18D Kit from Promega. The cell line sample was processed using the ABI Prism 3500xl Genetic Analyzer. Data were analyzed using GeneMapper ID-X v1.2 software (Applied Biosystems). Appropriate positive and negative controls were run and confirmed for each sample submitted.'

Data interpretation: Cell lines were authenticated using Short Tandem Repeat (STR) analysis as described in 2012 in ANSI Standard (ASN-0002) Authentication of Human Cell Lines: Standardization of STR Profiling by the ATCC Standards Development Organization (SDO)'

HeLa CCL-2 results: "Test Results: The submitted profile is an exact match for the following ATCC human cell line(s) in the ATCC STR database (eight core loci plus Amelogenin): CCL-2 (HeLa)'

M2 results: "Test Results: Submitted sample, STRA12409 (M2 melanoma), is an exact match to ATCC cell line CRL-2500 (A7). When compared to the reference profile the submitted profile shows and extra #10 allele at the TPOX locus. The cell line, (M2), has been discontinued by ATCC."

Mycoplasma monitoring: All cell lines were checked for potential mycoplasma infection using DAPI throughout the course of this study.

Plasmids—MIIA mEmerald (Addgene, Cambridge, MA, #54190), MIIA mApple (Addgene, #54929) and MIIB mEmerald (Addgene, #54192) were gifts from Michael Davidson. MIIA mEGFP (Addgene, #11347) was a gift from Robert Adelstein. MIIB mEGFP (Addgene, #35691) was a gift from Venkaiah Betapudi. The MIIB/A and MIIA/B chimeras were generously provided by Miguel Vincente Manzanares (Universidad Autonoma de Madrid, Spain).

siRNA resistant MIIB and MIIB/A were generated using a modified site directed mutagenesis protocol as described previously (Liu and Naismith, 2008). Three to four codons were modified to ensure siRNA resistance. The MIIB- and MIIB/A-mEGFP constructs were mutated using the following primer sequences- Forward- 5'-GGAAGACCCCGAGAGGTATCTCTTTGTGGACAGGGCTGT-3', Reverse- 5'-CTCTCGGGGTCTTCCAGTCCAGTTCTCTGCGCCAT-3'. Since the individual siRNA against MIIA was targeted to 3^0-UTR, the MIIA-mEGFP and MIIA/B-mEGFP plasmids were not mutated.

METHOD DETAILS

Phase and DIC imaging—Phase and DIC imaging was performed on a Nikon (Melville, NY) Eclipse Ti-E inverted microscope equipped with a Nikon 1.45 NA 100X Oil DIC, 0.95 NA 40X Air DIC and a 0.4 NA 20X Air Phase objective. Samples were maintained at 37C with 5% CO_2 using a Tokai Hit Stage Incubator (Shizuoka-ken, Japan).

For quantifying live binucleation events, imaging was performed on an Incucyte S3 (4647, Essen BioScience) microscope, equipped with a 20X objective and maintained in a tissue culture incubator at 37C and 5% CO_2.

Structured Illumination Microscopy (SIM)—SIM imaging was performed on a GE (Pittsburgh, PA) DeltaVision OMX microscope equipped with a 1.42 NA 60X objective lens and a sCMOS camera, and a Nikon N-SIM microscope equipped with a 1.49 NA 100X objective lens and an EMCCD camera.

Live and fixed fluorescence imaging and cortical ablation—Live imaging and cortical ablation were performed on a Nikon Eclipse Ti-E inverted microscope equipped with a Yokogawa CSU-X1 spinning disk head, 1.4 NA 60X oil objective, Andor DU-897 EMCCD and a dedicated 100 mW 405 diode ablation laser, generously provided by the Nikon Centre of Excellence at Vanderbilt University. The instrument was controlled using Nikon Elements AR software. For ablation, a 1.4 μm x 1.4 μm ROI was used for all experiments. A DIC and/or fluorescence image was acquired before ablation, followed by

ablation using a miniscanner. A pixel dwell time of 500 ms, 50% laser power was used for a duration of 1 s, followed by acquiring DIC or fluorescence images at 2 s intervals. Samples were maintained at 37°C with 5% CO_2 using Tokai Hit Stage Incubator.

To image MIIA and MIIB in fixed ESC colonies, large image stitching was performed using the 60X objective in Elements software. Z sections were acquired at 1 mm intervals for the entire stitch and maximum projections were displayed and used for generating line scans. To image endogenous MIIA and MIIB in fixed HeLa cells, single slices through the middle of the cell were acquired using the 60X objective.

Knockdown experiments—Smart Pool Accell siRNA against MIIA (myh9 gene, #E-007668, #1- CCGUUGACUCAGUAUAGUU, #2- UCCACAUCUUCUAUUAUCU, #3- GUGUGGUCAUCAAUCCUUA, #4- CUUAUGAGCUCCAAGGAUG) and MIIB (myh10 gene, #E-023017, #1- GGACUAAUCUAUA CUUAUU, #2- UGUCAAUGCUUAAAGUAGU, #3- CGAGGAUCCAGAGAGGUAU, #4- CCAAUUUACUCUGAGAAUA) were purchased from GE Dharmacon (Lafayette, CO). To perform rescue experiments, the following individual siRNAs were used- myh9 – CCGUUGA CUCAGUAUAGUU (#A-007668–13-0005) and myh10- CGAGGAUCCAGAGGUAU (#A-023015–15-0005). Knockdown experiments were performed in 24-well plates using Lipofectamine 2000 (Life Technologies, #1690146) as per instructions provided by the manufacturer. Knockdown was performed for 72 h, after which cells were either plated on the growth substrate for imaging or lysed for western blot experiments.

Western blotting—Gel samples were prepared by mixing cell lysates with LDS sample buffer (Life Technologies, #NP0007) and Sample Reducing Buffer (Life Technologies, #NP00009) and boiled at 95°C for 5 min. Samples were resolved on Bolt 4%–12% gradient Bis-Tris gels (Life Technologies, #NW04120BOX). Protein bands were blotted onto a nylon membrane (Millipore). Blots were blocked using 5% NFDM (Research Products International Corp, Mt. Prospect, IL, #33368) in Tris Buffered Saline with Tween-20 (TBST). Antibody incubations were also performed in 5% NFDM in TBST. Blots were developed using the Immobilon Chemiluminescence Kit (Millipore, #WBKLS0500).

Cell indentation assay—A precisely controlled Transfer Man 4R micromanipulator (Eppendorf, Hamburg, Germany) was magnetically attached to the optical table. Indentation pipettes were prepared from borosilicate microcapillary tubes pulled using an automated pipette puller. Metaphase cells were identified using high-magnification DIC and their height was approximated. The micropipette was then slowly lowered to gently rest on top of the cell. Upon starting image acquisition, the pipette was lowered continuously for 2 s, using the extra-fine movement setting, to compress the cell to half its height. Images were recorded for a minimum of 90 s prior to gently raising the pipette back up. The assay was performed in 35 mm glass bottom dishes with a 20 mm coverslip to allow for the optimal angle and movement of the microcapillary.

Micropipette aspiration—Microneedles (World Precision Instruments, 0.75 mm inner diameter and 1.0 mm outer diameter) were pulled to a centimeter-long taper using a

Narishige PC-100 needle puller. The following parameters were used- 55% maximum current and one light weight (mass = 23.5g). Using a Narishige MF-900 microforge, needles were then cut to a diameter ranging between 10–15 μm. The end of the needle was then fire polished by bringing it close to a heated glass bead to obtain a smooth edge that will successfully attach to the aspirated cell without disrupting the membrane. The microforge was then used to bend the tip of the micropipette needle to a 30-degree angle by positioning the needle vertically at a 0.1 mm distance from the heated glass bead.

To perform micropipette aspiration, the needles were mounted on an Eppendorf Transfer Man 4R micromanipulator that was magnetically attached to the optical table. Cells were visualized using DIC (Plan Apo 0.95 NA, 40X Nikon DIC air objective, with 1.5X optical zoom on a Nikon Eclipse Tiinverted microscope controlled using Elements software). Cells weremaintainedat37C with5%CO_2 using a Tokai Hit stage incubator. Metaphase cells were identified using the appearance of a tight metaphase plate using DIC. The needle was then positioned close to the cell until the pipette made firm contact with the cell. Negative pressure was then applied using a Fluigent microfluidic pressure control system (Flow EZ) controlled through Fluigent controller software on the microscope computer. Frames were acquired every 2 s, with pressure increased by0.5 mbar every 10 s.Cortex tension was then calculated by analyzing the DIC time montages using a custom MATLAB script (Data S1 and S2). Tension (T) was calculated as

$$T = \frac{\Delta P}{2\left(\frac{1}{Rp} - \frac{1}{Rc}\right)}$$

where, Δp = pressure difference, R_p = radius of pipette, R_c = radius of cell.

Calibration of protein expression using immunofluorescence—Calibration of protein expression was performed using an immunofluorescence based approach as described previously (Figure S9) (Taneja and Burnette, 2019). siRNA resistant MII was introduced into the knockdown cells using transient transfection, plated on glass coverslips, followed by fixation. Untransfected scrambled control cells were prepared in parallel. The two samples were then stained for endogenous MIIA or MIIB in the red channel. The samples were then imaged using the same parameters for the red and green channels in growth medium at 37C as performed for the actual experiment. GFP intensity measured in the cytoplasm was then calibrated against the endogenous (red) signal relative to the scrambled control. The intensity in the cytoplasm was also normalized against relative enrichment in the cytoplasm as well as background. This analysis was performed for every different objective lens used in the study. Since we used the same imaging parameters for GFP throughout the experiments, this allowed us to compare levels to endogenous.

Quantification of soluble and insoluble fractions in HAP1 fibroblasts—HAP1 parental fibroblasts were seeded into 24-well culture plates (CytoOne CC7682–7524) and grown to 75% confluence. Cells were then trypsinized, followed by recovery in growth medium on an orbital shaker for 10 min. Cells were pelleted at 200xg, washed once in PBS, and then lysed using Cell Lytic M reagent (Sigma C2978) containing 1X protease inhibitor

cocktail (Sigma P8340) for 45 min on ice. Cell lysates were centrifuged for 10 min at 15000 rpm at 4C. The supernatant (soluble fraction) was diluted in LDS Sample buffer (Life Technologies #NP0007) and Reducing buffer (Life Technologies #NP00009). The pellet (insoluble fraction) was the resuspended in LDS Sample Buffer and Reducing buffer. The two fractions were boiled at 95C for 5 min and subsequently analyzed by western blotting. Note that the actual fractions obtained by this method may vary from previous reports (Schiffhauer et al., 2019) since we did not use ATP in our lysis buffer, which would promote release of MII from the insoluble fraction into the soluble fraction. Therefore, our values for the insoluble fraction tend to be higher.

QUANTIFICATION AND STATISTICAL ANALYSIS

Data quantification—For quantification of MII stack length (Figures 1A–1C), a 15 μm by 8 μm region of interest containing the cleavage furrow was cropped from maximum projected SIM micrographs. Owing to the smaller size of HAP1 fibroblasts, a 5 μm by 8 μm region of interest containing the cleavage furrow was used. Only bright, in-focus, objects were included in the analysis. Measurements were made manually with individual lines saved as ROIs in Fiji and then exported for calculation of average stack length. Separate investigators acquired and analyzed the data for stack length quantification. The investigator analyzing the data were blinded.

For measuring the rate of cleavage furrow ingression, phase contrast or DIC time montages were recorded at 30 s intervals. Individual montages were cropped and aligned using the StackReg plugin in Fiji. Kymographs were created using the Multiple Kymograph plugin with a 3-pixel thick line drawn across the equator. Ingression rates were calculated as the change in distance (in mm) divided by the amount of time (in min) between the start and end of ingression (Figure 1D). The start of ingression was defined as the first instance of deformation of the cell boundary, and the end of ingression was defined as when the cell boundary stopped deforming. Asymmetric furrowing was occasionally observed in HAP1 fibroblasts. In these instances, the predominant side of the cleavage furrow was measured. In the case of symmetrical ingression, the left side of the kymograph was arbitrarily used (Figure 1D).

To quantify blebbing (Figure 2), DIC time-lapse recordings at 30 s intervals were used. We manually counted blebs using the line tool in Fiji, between the time point immediately following the end of Anaphase A (sister chromatids no longer move away from each other; this was also verified by making a kymograph across the long axis of the cytokinetic cell) and the end of cleavage furrow ingression. The longest axis of every bleb (most frequently the diameter since blebs were roughly circular in shape) that was in focus and could be accurately measured was counted for quantification. The diameter of every bleb measured for the duration of the movie was summed. This was then normalized to the number of min for which the analysis was performed.

To quantify ingression rates within hESC colonies (Figure S3), images were recorded at 30 s intervals. Distance within the colony was measured in “cell radii” from the edge. The colonies were assumed to be composed of concentric circular cell layers increasing in number from the edge. For any given dividing cell, its position was determined by counting

the smallest number of cell radii to reach the edge. Ingression rates were measured using the MultipleKymograph plugin in Fiji. Kymographs where the cell boundary could not be ascertained were discarded.

To quantify cell shape changes upon MII knockdown (Figure 2), we measured the increase in pole-to-pole elongation during cytokinesis relative to metaphase. A line was drawn across the long axis of the cell from phase contrast time montages. We observed that the distance between the cell boundary during metaphase is smallest immediately before the onset of anaphase, which is in agreement with the general idea that maximal de-adhesion must occur for cell-cycle progression (Jones et al., 2018; Marchesi et al., 2014). Following anaphase onset, pole-to-pole expansion was observed, until ingression is completed, which was then followed by poles moving closer together again prior to cell spreading. We measured the pole-to-pole distance immediately upon anaphase onset (as shown in schematic, Figure 2), and the maximal pole-to-pole distance before they come closer together (as shown in schematic, Figure 2). This was also visually confirmed in the live cell montages. These widths were used to calculate the pole-to-pole elongation ratio.

To generate the endogenous polar cortex and equatorial cortex localization profiles upon MII paralog knockdown (Figures 3A–3C), cells were grouped into early (> 20 μm), mid (6–20 μm) and late cytokinesis (< 6 μm) based on degree of furrow closure, as done previously (Taneja et al., 2016). Polar cortex intensity was calculated as the mean fluorescence averaged from 6 ROIs (1.8 μm^2 area) placed in the same positions (see inset schematics, Figure 3). Due to the non-uniform distribution of cortical signals, this approach allowed us to get an unbiased measurement of mean cortical intensity at the polar cortex. Equatorial cortex intensity was calculated as mean fluorescence of 2 ROIs (1.8 μm^2 area) placed on each side of the furrow. Mean equatorial or polar cortex intensities were then averaged within the cytokinesis groups. Any perturbations were normalized to the mean of the control datasets.

To quantify changes in filament composition upon MII paralog depletion (Figure 3), two-channel images SIM were first aligned in all dimensions in Fiji. Following alignment, a 5 μm by 15 μm crop from a single optical section from the 2-channel overlay was used for quantification of hetero-filaments at the cortex. Each distinct punctum was quantified as a filament. In instances of puncta located close together, a line scan was drawn across region, and each distinct peak in intensity was quantified as a filament. Puncta localized in the cytoplasm were not counted. The same staining and imaging parameters were used for all the experiments to allow comparison of MII intensity within the filaments.

For quantification of binucleate cells (Figure 6), a large stitch of cells stained with phalloidin and DAPI was acquired using a 20X objective (shown in Figure S1C or smaller field of view shown in in Figure 6A). Binucleate cells were manually counted using the multi-point tool in Fiji. Cells very close together in clusters and whose boundaries could not be accurately discerned were not included in the analysis.

To correlate spindle displacement with blebbing (Figure 7B), DIC time-lapse imaging was performed at 5 s intervals. A 3-pixel thick line was drawn parallel to the long axis of the

cytokinetic cell and kymographs were created using the Multiple Kymograph plugin in Fiji. The pixel values for the time point at which bleb growth was maximal was noted, in parallel with the pixel value for the time point at which the chromosomes were displaced to the maximal extent. The plot in Figure 7B was created by plotting all such events across multiple cells.

To quantify the different modes of binucleation (Figure 7F), live imaging of MIIB^{lo} cells was performed as follows. Cells were seeded on 24-well cell culture dishes. Knockdown was performed 24 h following seeding. 48 h after initiation of knockdown, live nuclear labeling was performed using the NucLight Red reagent (used at a dilution of 1/2000 in DMEM) for 6 h prior to imaging. Time lapse montages were acquired at 20X magnification at 10-minute intervals. A binucleation event was classified as “chromosome missegregation without abscission” if, i) a clear frame was observed where the DNA signal was detected in only one daughter cell, ii) the boundary between the daughter cells could be clearly discerned. A binucleation event was classified as “abscission failure” if, i) no frame was observed where the DNA signal was detected in only one daughter cell, ii) the daughter cells fail to separate with or without the appearance of a midbody. Events showing both of the above features were classified as “chromosome missegregation with abscission failure.

Statistics—Statistical significance for averaged data from multiple experiments, which is always depicted using bar graphs, was determined using unpaired, 2-tailed, homoscedastic Student’s t test performed on Excel. For data pooled from multiple experiments, always depicted as Tukey plots, Mann Whitney U-test was performed on GraphPad Prism. Error bars in all bar graphs represent standard error of the mean, while Tukey plots were represented with boxes (with median, Q1, Q3 percentiles), whiskers (minimum and maximum values within 1.5 times interquartile range) and outliers (solid circles). No outliers were removed from the analysis.

For graphs displaying percentages, no error bar was displayed and the data over more than 3 experiments was pooled. Due to the pooled approach for the endogenous MII localizations in HeLa cells, error bars depict standard error of weighted means, where the weights were determined based on how many cells from a particular experimental replicate were allocated to a particular group (e.g., Early, Mid, Late). The weighted standard deviation was calculated to remove any bias from individual experiments, using the formula

$$sd_w = \sqrt{\frac{\sum_{i=1}^{N} w_i (x_i - \bar{x}_w)^2}{\frac{(N' - 1)\sum_{i=1}^{N} w_i}{N}}}$$

where w_i is the weight for the i^{th} observation, N’ is the number of non-zero weights, and x_w is the weighted mean of the observations

DATA AND CODE AVAILABILITY

The published article includes all code generated during this study.

Supplementary Material

Refer to Web version on PubMed Central for supplementary material.

ACKNOWLEDGMENTS

We thank David Miller for providing glass micro-capillaries for the indentation assay; Miguel Vincente-Manzanares for providing MII chimeras; Nikon Center of Excellence, Vanderbilt University for access to the Nikon Spinning Disk microscope and technical support; Kristopher Burkewitz for lending his InjectMan for micro-pipette aspiration; and the Vanderbilt Mass Spectrometry Core Lab for assistance with quantification of paralog levels in HAP1 cells. This work was funded by a Maximizing Investigators' Research Award (MIRA) from the National Institute of General Medical Sciences (NIGMS) (R35 GM125028-01 to D.T.B.); an American Heart Association Predoctoral Fellowship (18PRE33960551 to N.T.); a MIRA (R35-GM128915 to V.G.); and a MIRA (R35-HL135790 to W.D.M. and R01-GM086610 to R.O.).

REFERENCES

Beach JR, Shao L, Remmert K, Li D, Betzig E, and Hammer JA 3rd. (2014). Nonmuscle myosin II isoforms coassemble in living cells. Curr. Biol 24, 1160–1166. [PubMed: 24814144]

Bekker-Jensen DB, Kelstrup CD, Batth TS, Larsen SC, Haldrup C, Bramsen JB, Sorensen KD, Hoyer S, Orntoft TF, Andersen CL, et al. (2017). An optimized shotgun strategy for the rapid generation of comprehensive human proteomes. Cell Syst. 4, 587–599 e584.

Bement WM, Leda M, Moe AM, Kita AM, Larson ME, Golding AE, Pfeuti C, Su KC, Miller AL, Goryachev AB, and von Dassow G (2015). Activator-inhibitor coupling between Rho signalling and actin assembly makes the cell cortex an excitable medium. Nat. Cell Biol 17, 1471–1483. [PubMed: 26479320]

Bovellan M, Romeo Y, Biro M, Boden A, Chugh P, Yonis A, Vaghela M, Fritzsche M, Moulding D, Thorogate R, et al. (2014). Cellular control of cortical actin nucleation. Curr. Biol 24, 1628–1635. [PubMed: 25017211]

Brugués J, Maugis B, Casademunt J, Nassoy P, Amblard F, and Sens P (2010). Dynamical organization of the cytoskeletal cortex probed by micropipette aspiration. Proc. Natl. Acad. Sci. USA 107, 15415–15420. [PubMed: 20713731]

Carreno S, Kouranti I, Glusman ES, Fuller MT, Echard A, and Payre F (2008). Moesin and its activating kinase Slik are required for cortical stability and microtubule organization in mitotic cells. J. Cell Biol 180, 739–746. [PubMed: 18283112]

Charras G, and Paluch E (2008). Blebs lead the way: how to migrate without lamellipodia. Nat. Rev. Mol. Cell Biol 9, 730–736. [PubMed: 18628785]

Charras GT, Hu CK, Coughlin M, and Mitchison TJ (2006). Reassembly of contractile actin cortex in cell blebs. J. Cell Biol 175, 477–490. [PubMed: 17088428]

Cunningham CC (1995). Actin polymerization and intracellular solvent flow in cell surface blebbing. J. Cell Biol 129, 1589–1599. [PubMed: 7790356]

Dasbiswas K, Hu S, Bershadsky AD, and Safran SA (2019). Registry kinetics of myosin motor stacks driven by mechanical force-induced actin turnover. Biophys. J 117, 856–866. [PubMed: 31427069]

Fenix AM, Taneja N, Buttler CA, Lewis J, Van Engelenburg SB, Ohi R, and Burnette DT (2016). Expansion and concatenation of non-muscle myosin IIA filaments drive cellular contractile system formation during interphase and mitosis. Mol. Biol. Cell, mbc.E15–10-0725.

Fishkind DJ, and Wang YL (1993). Orientation and three-dimensional organization of actin filaments in dividing cultured cells. J. Cell Biol 123, 837–848. [PubMed: 8227144]

Friedrich BM, Buxboim A, Discher DE, and Safran SA (2011). Striated acto-myosin fibers can reorganize and register in response to elastic interactions with the matrix. Biophys. J 100, 2706–2715. [PubMed: 21641316]

Fritzsche M, Erlenkämper C, Moeendarbary E, Charras G, and Kruse K (2016). Actin kinetics shapes cortical network structure and mechanics. Sci. Adv 2, e1501337.

Fujiwara K, and Pollard TD (1976). Fluorescent antibody localization of myosin in the cytoplasm, cleavage furrow, and mitotic spindle of human cells. J. Cell Biol 71, 848–875. [PubMed: 62755]

Gardel ML, Kasza KE, Brangwynne CP, Liu J, and Weitz DA (2008). Chapter 19: Mechanical response of cytoskeletal networks. Methods Cell Biol. 89, 487–519. [PubMed: 19118688]

Gardel ML, Schneider IC, Aratyn-Schaus Y, and Waterman CM (2010). Mechanical integration of actin and adhesion dynamics in cell migration. Annu. Rev. Cell Dev. Biol 26, 315–333. [PubMed: 19575647]

Goudarzi M, Banisch TU, Mobin MB, Maghelli N, Tarbashevich K, Strate I, van den Berg J, Blaser H, Bandemer S, Paluch E, et al. (2012). Identification and regulation of a molecular module for bleb-based cell motility. Dev. Cell 23, 210–218. [PubMed: 22705393]

Guha M, Zhou M, and Wang YL (2005). Cortical actin turnover during cytokinesis requires myosin II. Curr. Biol 15, 732–736. [PubMed: 15854905]

Heer NC, and Martin AC (2017). Tension, contraction and tissue morphogenesis. Development 144, 4249–4260. [PubMed: 29183938]

Jonckheere V, Fija1kowska D, and Van Damme P (2018). Omics assisted N-terminal proteoform and protein expression profiling on methionine aminopeptidase 1 (MetAP1) deletion. Mol. Cell. Proteomics 17, 694–708. [PubMed: 29317475]

Jones MC, Askari JA, Humphries JD, and Humphries MJ (2018). Cell adhesion is regulated by CDK1 during the cell cycle. J. Cell Biol 217, 3203–3218. [PubMed: 29930204]

Kanada M, Nagasaki A, and Uyeda TQ (2005). Adhesion-dependent and contractile ring-independent equatorial furrowing during cytokinesis in mammalian cells. Mol. Biol. Cell 16, 3865–3872. [PubMed: 15944220]

Kee YS, and Robinson DN (2013). Micropipette aspiration for studying cellular mechanosensory responses and mechanics. Methods Mol. Biol 983, 367–382. [PubMed: 23494318]

Kovács M, Wang F, Hu A, Zhang Y, and Sellers JR (2003). Functional divergence of human cytoplasmic myosin II: kinetic characterization of the non-muscle IIA isoform. J. Biol. Chem 278, 38132–38140. [PubMed: 12847096]

Levayer R, and Lecuit T (2012). Biomechanical regulation of contractility: spatial control and dynamics. Trends Cell Biol. 22, 61–81. [PubMed: 22119497]

Liu H, and Naismith JH (2008). An efficient one-step site-directed deletion, insertion, single and multiple-site plasmid mutagenesis protocol. BMC Biotechnol. 8, 91. [PubMed: 19055817]

Lordier L, Bluteau D, Jalil A, Legrand C, Pan J, Rameau P, Jouni D, Bluteau O, Mercher T, Leon C, et al. (2012). RUNX1-induced silencing of non-muscle myosin heavy chain IIB contributes to megakaryocyte polyploidization. Nat. Commun 3, 717. [PubMed: 22395608]

Machacek M, Hodgson L, Welch C, Elliott H, Pertz O, Nalbant P, Abell A, Johnson GL, Hahn KM, and Danuser G (2009). Coordination of Rho GTPase activities during cell protrusion. Nature 461, 99–103. [PubMed: 19693013]

Maddox AS, and Burridge K (2003). RhoA is required for cortical retraction and rigidity during mitotic cell rounding. J. Cell Biol 160, 255–265. [PubMed: 12538643]

Marchesi S, Montani F, Deflorian G, D'Antuono R, Cuomo A, Bologna S, Mazzoccoli C, Bonaldi T, Di Fiore PP, and Nicassio F (2014). DEPDC1B coordinates de-adhesion events and cell-cycle progression at mitosis. Dev. Cell 31, 420–433. [PubMed: 25458010]

Martin AC, Kaschube M, and Wieschaus EF (2009). Pulsed contractions of an actin-myosin network drive apical constriction. Nature 457, 495–499. [PubMed: 19029882]

Melli L, Billington N, Sun SA, Bird JE, Nagy A, Friedman TB, Takagi Y, and Sellers JR (2018). Bipolar filaments of human nonmuscle myosin 2-A and 2-B have distinct motile and mechanical properties. eLife 7, 7.

Milberg O, Shitara A, Ebrahim S, Masedunskas A, Tora M, Tran DT, Chen Y, Conti MA, Adelstein RS, Ten Hagen KG, and Weigert R (2017). Concerted actions of distinct nonmuscle myosin II isoforms drive intracellular membrane remodeling in live animals. J. Cell Biol 216, 1925–1936. [PubMed: 28600434]

Murakami N, Singh SS, Chauhan VP, and Elzinga M (1995). Phospholipid binding, phosphorylation by protein kinase C, and filament assembly of the COOH terminal heavy chain fragments of

nonmuscle myosin II isoforms MIIA and MIIB. Biochemistry 34, 16046–16055. [PubMed: 8519761]

Murrell MP, and Gardel ML (2012). F-actin buckling coordinates contractility and severing in a biomimetic actomyosin cortex. Proc. Natl. Acad. Sci. USA 109, 20820–20825. [PubMed: 23213249]

Nakasawa T, Takahashi M, Matsuzawa F, Aikawa S, Togashi Y, Saitoh T, Yamagishi A, and Yazawa M (2005). Critical regions for assembly of vertebrate nonmuscle myosin II. Biochemistry 44, 174–183. [PubMed: 15628858]

Neujahr R, Heizer C, and Gerisch G (1997). Myosin II-independent processes in mitotic cells of Dictyostelium discoideum: redistribution of the nuclei, re-arrangement of the actin system and formation of the cleavage furrow. J. Cell Sci 110, 123–137. [PubMed: 9044043]

Paluch E, Piel M, Prost J, Bornens M, and Sykes C (2005). Cortical actomyosin breakage triggers shape oscillations in cells and cell fragments. Biophys. J 89, 724–733. [PubMed: 15879479]

Rosenfeld SS, Xing J, Chen LQ, and Sweeney HL (2003). Myosin IIb is unconventionally conventional. J. Biol. Chem 278, 27449–27455. [PubMed: 12740390]

Salbreux G, Charras G, and Paluch E (2012). Actin cortex mechanics and cellular morphogenesis. Trends Cell Biol. 22, 536–545. [PubMed: 22871642]

Sandquist JC, and Means AR (2008). The C-terminal tail region of non-muscle myosin II directs isoform-specific distribution in migrating cells. Mol. Biol. Cell 19, 5156–5167. [PubMed: 18843042]

Schiffhauer ES, Ren Y, Iglesias VA, Kothari P, Iglesias PA, and Robinson DN (2019). Myosin IIB assembly state determines its mechanosensitive dynamics. J. Cell Biol 218, 895–908. [PubMed: 30655296]

Sedzinski J, Biro M, Oswald A, Tinevez JY, Salbreux G, and Paluch E (2011). Polar actomyosin contractility destabilizes the position of the cytokinetic furrow. Nature 476, 462–466. [PubMed: 21822289]

Sezgin E, Levental I, Mayor S, and Eggeling C (2017). The mystery of membrane organization: composition, regulation and roles of lipid rafts. Nat. Rev. Mol. Cell Biol 18, 361–374. [PubMed: 28356571]

Shutova MS, Spessott WA, Giraudo CG, and Svitkina T (2014). Endogenous species of mammalian nonmuscle myosin IIA and IIB include activated monomers and heteropolymers. Curr. Biol 24, 1958–1968. [PubMed: 25131674]

Stam S, Alberts J, Gardel ML, and Munro E (2015). Isoforms confer characteristic force generation and mechanosensation by Myosin II filaments. Biophys. J 108, 1997–2006. [PubMed: 25902439]

Stewart MP, Helenius J, Toyoda Y, Ramanathan SP, Muller DJ, and Hyman AA (2011). Hydrostatic pressure and the actomyosin cortex drive mitotic cell rounding. Nature 469, 226–230. [PubMed: 21196934]

Straight AF, Field CM, and Mitchison TJ (2005). Anillin binds nonmuscle myosin II and regulates the contractile ring. Mol. Biol. Cell 16, 193–201. [PubMed: 15496454]

Surcel A, Kee YS, Luo T, and Robinson DN (2010). Cytokinesis through biochemical-mechanical feedback loops. Semin. Cell Dev. Biol 21, 866–873. [PubMed: 20709619]

Surcel A, Schiffhauer ES, Thomas DG, Zhu Q, DiNapoli KT, Herbig M, Otto O, West-Foyle H, Jacobi A, Krä ter M, Plak K, et al. (2019). Targeting mechanoresponsive proteins in pancreatic cancer: 4-hydroxyacetophenone blocks dissemination and invasion by activating MYH14. Cancer Research 79, 4665–4678. [PubMed: 31358530]

Taneja N, and Burnette DT (2019). Myosin IIA drives membrane bleb retraction. Mol. Biol. Cell 30, 1051–1059. [PubMed: 30785846]

Taneja N, Fenix AM, Rathbun L, Millis BA, Tyska MJ, Hehnly H, and Burnette DT (2016). Focal adhesions control cleavage furrow shape and spindle tilt during mitosis. Sci. Rep 6, 29846. [PubMed: 27432211]

Tinevez JY, Schulze U, Salbreux G, Roensch J, Joanny JF, and Paluch E (2009). Role of cortical tension in bleb growth. Proc. Natl. Acad. Sci. USA 106, 18581–18586. [PubMed: 19846787]

Vicente-Manzanares M, Koach MA, Whitmore L, Lamers ML, and Horwitz AF (2008). Segregation and activation of myosin IIB creates a rear in migrating cells. J. Cell Biol 183, 543–554. [PubMed: 18955554]

Wang F, Kovacs M, Hu A, Limouze J, Harvey EV, and Sellers JR (2003). Kinetic mechanism of non-muscle myosin IIB: functional adaptations for tension generation and maintenance. J. Biol. Chem 278, 27439–27448. [PubMed: 12704189]

Wang K, Wloka C, and Bi E (2019). Non-muscle Myosin-II is required for the generation of a constriction site for subsequent abscission. iScience 13, 69–81. [PubMed: 30825839]

Yamamoto K, Otomo K, Nemoto T, Ishihara S, Haga H, Nagasaki A, Murakami Y, and Takahashi M (2019). Differential contributions of non-muscle myosin IIA and IIB to cytokinesis in human immortalized fibroblasts. Exp. Cell Res 376, 67–76. [PubMed: 30711568]

Zemel A, Rehfeldt F, Brown AE, Discher DE, and Safran SA (2010). Optimal matrix rigidity for stress fiber polarization in stem cells. Nat. Phys 6, 468–473. [PubMed: 20563235]

Highlights

- Myosin-IIA templates myosin-II filament stacks for faster cleavage furrow ingression
- Myosin-IIA generates cortex tension while myosin-IIB acts as a cortex stabilizer
- Cortex tension is tuned by composition of myosin-IIA/B hetero-filaments
- MIIB regulates cytokinetic fidelity through two distinct mechanisms

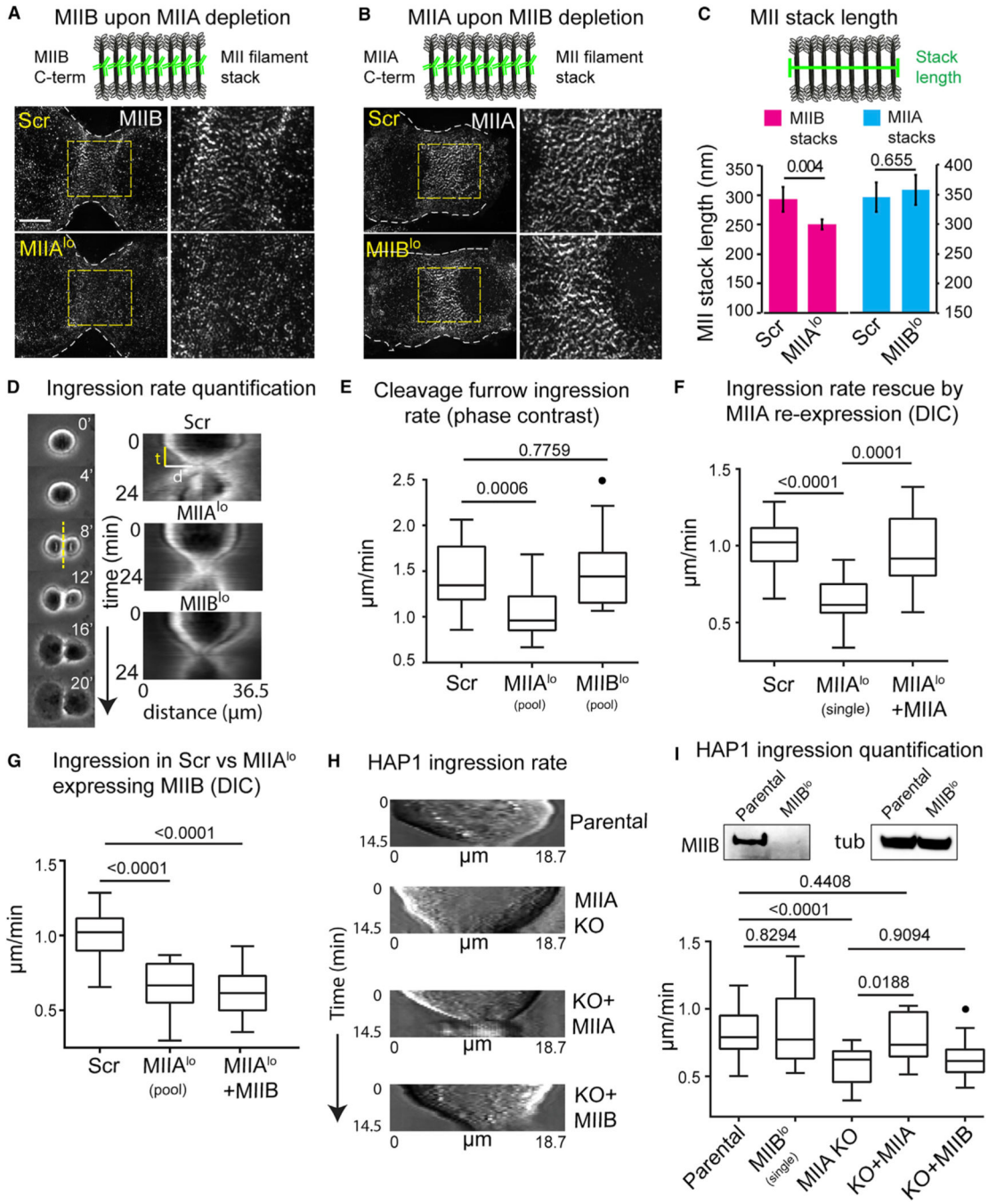

Figure 1. MIIA Drives Furrow Ingression through Templating of MII Stacks

(A and B) Endogenous MIIB (A) and MIIA (B) in the cleavage furrow of Scr versus MIIA^{lo} or MIIB^{lo} cells, respectively. (Insets) Zoom of yellow box. For (A), n = 13 Scr cells, N = 4 experiments; n = 17 MIIA^{lo} cells, N = 5 experiments. For (B), n = 14 Scr and 8 MIIB^{lo} cells, N = 3 experiments. Schematic, labeling strategy.

(C)Average length of MII stacks.

(D) Furrow ingression rate from phase contrast at 20× magnification.

(E) Tukey plots of ingression from phase contrast. n = 18 Scr, 22 MIIA^{lo} (pooled siRNA) and 20 MIIB^{lo} (pooled siRNA) cells, N = 3 experiments.
(F) Tukey plots of ingression measured independently using DIC at 60× magnification. n = 18 Scr, 16 MIIA^{lo} (single siRNA), and 14 MIIA^{lo}+MIIA cells, N = 4 experiments. (Note: phase contrast systematically overestimates distance measurements and gives higher values of ingression. Hence, the y axis is scaled differently for E.)
(G) Tukey plots of ingression measured independently using DIC. n = 15 MIIA^{lo} (pooled siRNA) and 15 MIIA^{lo}+MIIB cells, N = 3 experiments. The Scr dataset is the same as (F) and is only displayed for comparison.
(H) Representative kymographs of parental, MIIA-KO, MIIA-KO+MIIA-mEGFP, and MIIA-KO+MIIB-mEGFP HAP1 cells.
(I) Tukey plots of ingression for parental, MIIB^{lo} (single siRNA), MIIA-KO, MIIA-KO +MIIA-mEGFP, or MIIA-KO+MIIB-mEGFP HAP1 fibroblasts. n = 11 MIIA KO, 12 MIIA-expressing, and 10 MIIB-expressing cells, N = 3 experiments. Solid circles represent outliers. (Inset) Western blot showing siRNA knockdown of MIIB in parental HAP1 fibroblasts with tubulin as loading control. Error bars in (C) represent standard error of the means. Scale bar, 5 mm. p values stated over graphs.

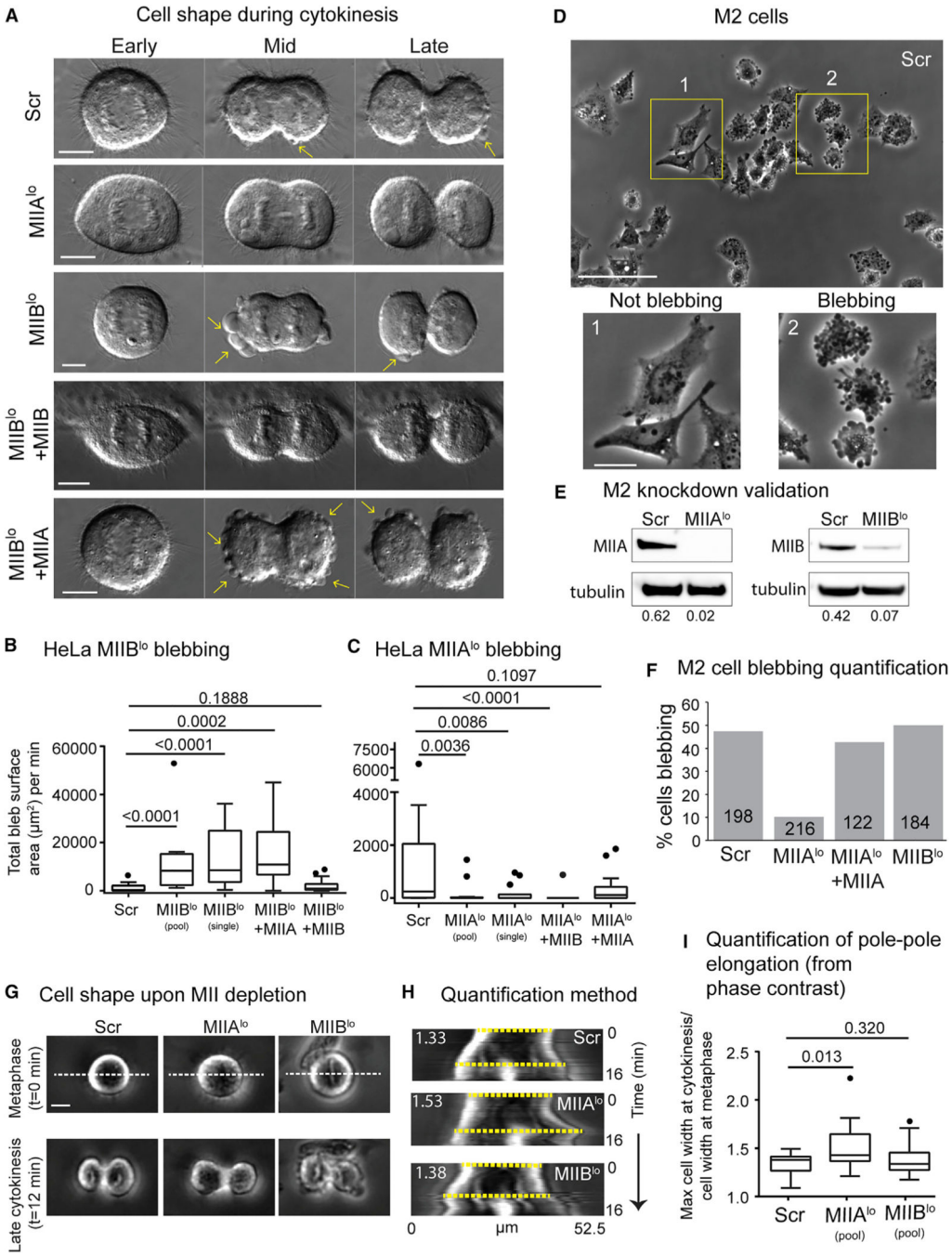

Figure 2. MII Paralog Depletion Leads to Distinct Alterations to Cell Shape

(A) Early, mid, and late cytokinesis in Scr, MIIB^{lo}, MIIA^{lo}, MIIB^{lo}+ MIIB-mEGFP, and MIIB^{lo}+ MIIA-mEGFP cells. Yellow arrows denote blebs.

(B and C) Tukey plots of blebbing measured as sum diameter of blebs per minute.

(B) n = 18 Scr, 15 MIIB^{lo} (pooled siRNA), 16 MIIB^{lo} (single siRNA), 15 MIIB^{lo} +MIIB, and 10 MIIB^{lo} +MIIA cells, N = 4 experiments.

(C) n = 14 MIIA^{lo} (pooled siRNA), 14 MIIA^{lo} (single siRNA), 14 MIIA^{lo} +MIIA, and 15 MIIA^{lo} +MIIB cells; N = 4 experiments.

(D) Control M2 cells 5-h post plating. (Insets) Examples of not-blebbing (1) versus blebbing (2) cells.
(E) Knockdown of MIIA and MIIB in M2 cells. Intensity of MII bands normalized to tubulin loading control shown below each band.
(F) Proportion of blebbing cells in Scr, MIIA^{lo}, MIIB^{lo}, or MIIA^{lo}+MIIA-mEGFP. Number of cells stated inside bars.
(G) Scr, MIIA^{lo}, and MIIB^{lo} cells at metaphase and late cytokinesis.
(H) Kymographs were generated using dotted white lines in (G). Dotted yellow lines show the two pole-to-pole lengths used to measure elongation ratio. SeeMethod Details for quantification details.
(I) Tukey plots of polar elongation. n = 17 Scr, 20 MIIA^{lo} (pooled siRNA) and 18 MIIB^{lo} (pooled siRNA) cells, N = 3 experiments.
Scale bars, (A) and (G) 10 μm; (D) 100 μm; (inset) 25 μm. p values stated over graphs.

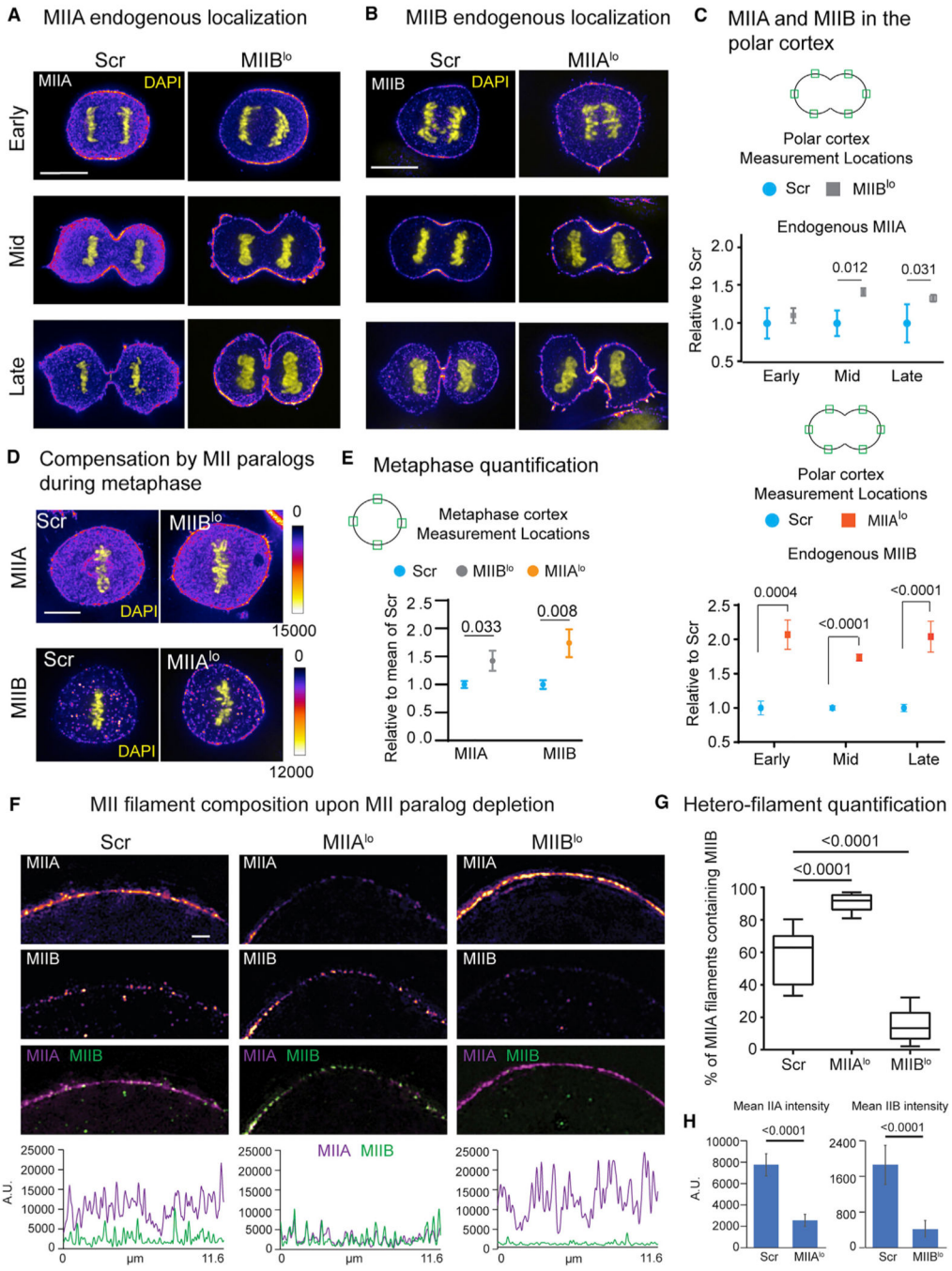

Figure 3. MII Paralog Compensation at the Polar Cortex upon MII Knockdown Results in Altered Hetero-Filament Composition

(A and B) Early, mid, and late cytokinesis cells showing endogenous MIIA (A) or MIIB (B) (Fire LUT) in Scr versus MIIB^{lo} or MIIA^{lo} cells, respectively. All compared images were scaled similarly.

(C) Intensity of MIIA and MIIB at the polar cortex calculated as mean of green regions of interest (ROIs) in cartoon insets. For MIIA: n = 41 Scr and 48 MIIB^{lo} cells, N = 3 experiments. For MIIB: n = 46 Scr and 43 MIIA^{lo} cells, N = 3 experiments.

(D) MIIA and MIIB localization (Fire LUT) during metaphase in MIIB^{lo} and MIIA^{lo} cells, respectively.
(E) MIIA: n = 15 cells each for Scr and MIIB^{lo}, N = 3 experiments. MIIB: n = 13 Scr cells and 12 MIIA^{lo} cells, N = 3 experiments.
(F) MIIA and MIIB localization (mpl inferno LUT for single channel) in control versus knockdown cells using SIM.
(G) Tukey plots showing percentage of MIIA filaments that co-localized with MIIB. Solid circles represent outliers.
(H) Mean intensity of MIIA and MIIB upon knockdown. n = 503, 361, and 354 filaments in Scr, MIIA^{lo} and MIIB^{lo} cells, respectively, from 10 cells per condition; N = 3 experiments. Error bars in (C) and (E) represent standard error of weighted mean. Error bars in (H) represent standard error of the means. Scale bars, (A), (B), and (D) 10 μm; (F) 1 μm. p values stated over graphs.

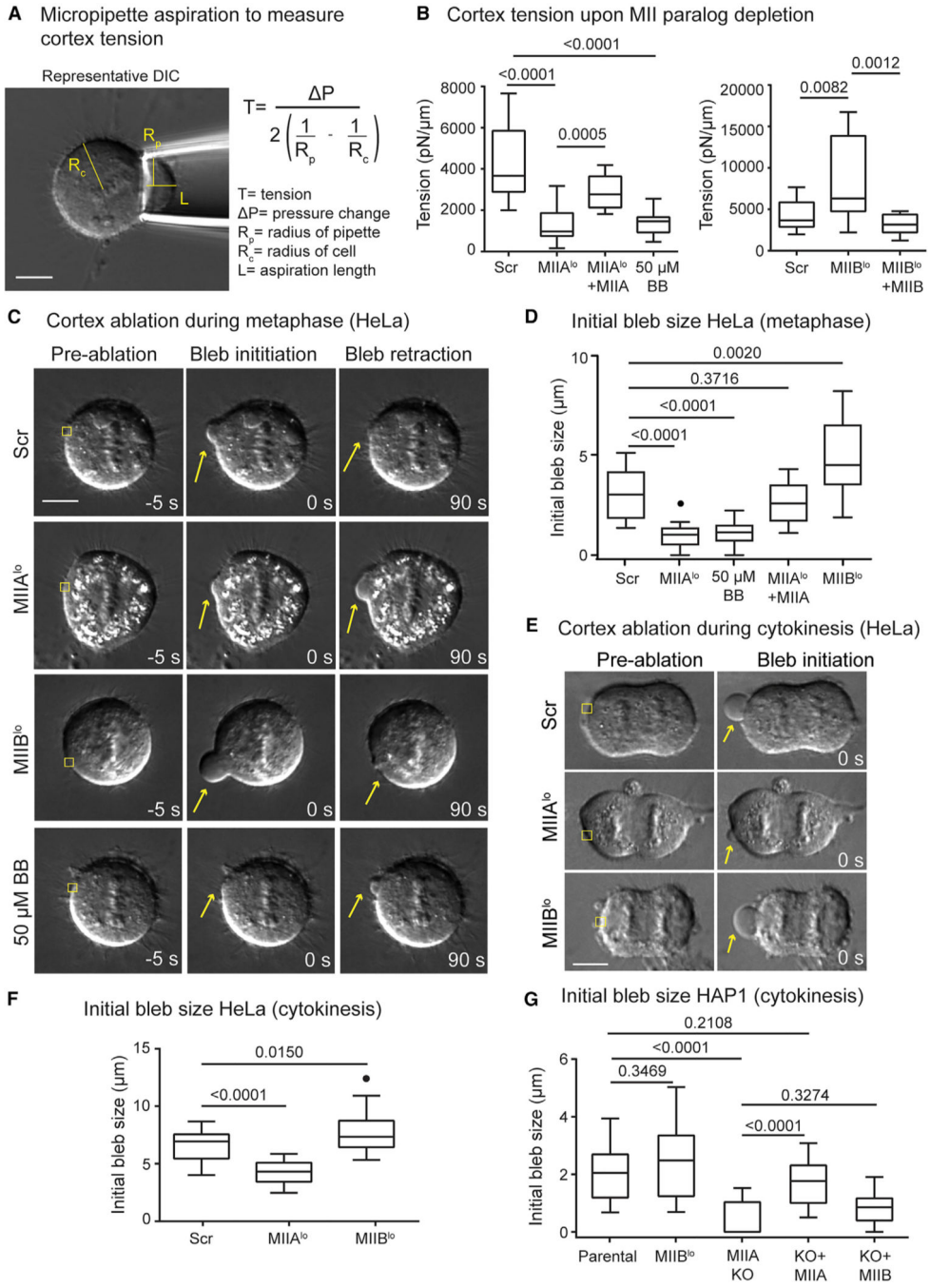

Figure 4. MIIA Is Necessary and Sufficient to Generate Cortex Tension and Intracellular Pressure

(A) Micropipette aspiration of control cell during metaphase, showing cell radius (R_c), aspirated length (L), and radius of pipette (R_p). Tension was calculated using the mathematical expression shown.

(B) Tukey plots of cortex tension upon MII paralog depletion. n = 16 Scr, 14 MIIA^{lo}, 15 MIIB^{lo}, 10 MIIA^{lo} +MIIA-mEGFP, 11 blebbistatin-treated, and 12 MIIB^{lo} +MIIB-mEGFP cells, N = 4 experiments each.

(C) Scr, MIIA^{lo}, MIIB^{lo}, and 50 μM of blebbistatin-treated HeLa cells before ablation, 0 s after ablation, and 90 s after ablation of the metaphase cortex. Yellow squares depict ablation ROI, yellow arrows depict blebs.

(D) Tukey plots showing initial bleb size during metaphase in HeLa cells. n = 17 Scr, 16 MIIA^{lo}, 14 MIIA^{lo} +MIIA, 14 50-mM blebbistatin-treated, and 18 MIIB^{lo} cells, N = 3 experiments.

(E) Polar cortex ablation in Scr, MIIA^{lo}, and MIIB^{lo} HeLa cells during cytokinesis. Yellow squares depict ablation ROI, yellow arrows denote bleb created by ablation.

(F) Tukey plots of initial bleb size during cytokinesis in HeLa cells. n = 25 Scr, 15 MIIA^{lo}, and 25 MIIB^{lo} cells, N = 3 experiments.

(G) Tukey plots of initial bleb size following ablation in HAP1 KO fibroblasts during cytokinesis. n = 12 untransfected MIIA-KO-, 26 MIIA-, and 11 MIIB-expressingcells, N = 3 experiments.

Scale bars, 10 mm. Solid circles represent outliers. p values stated over graphs.

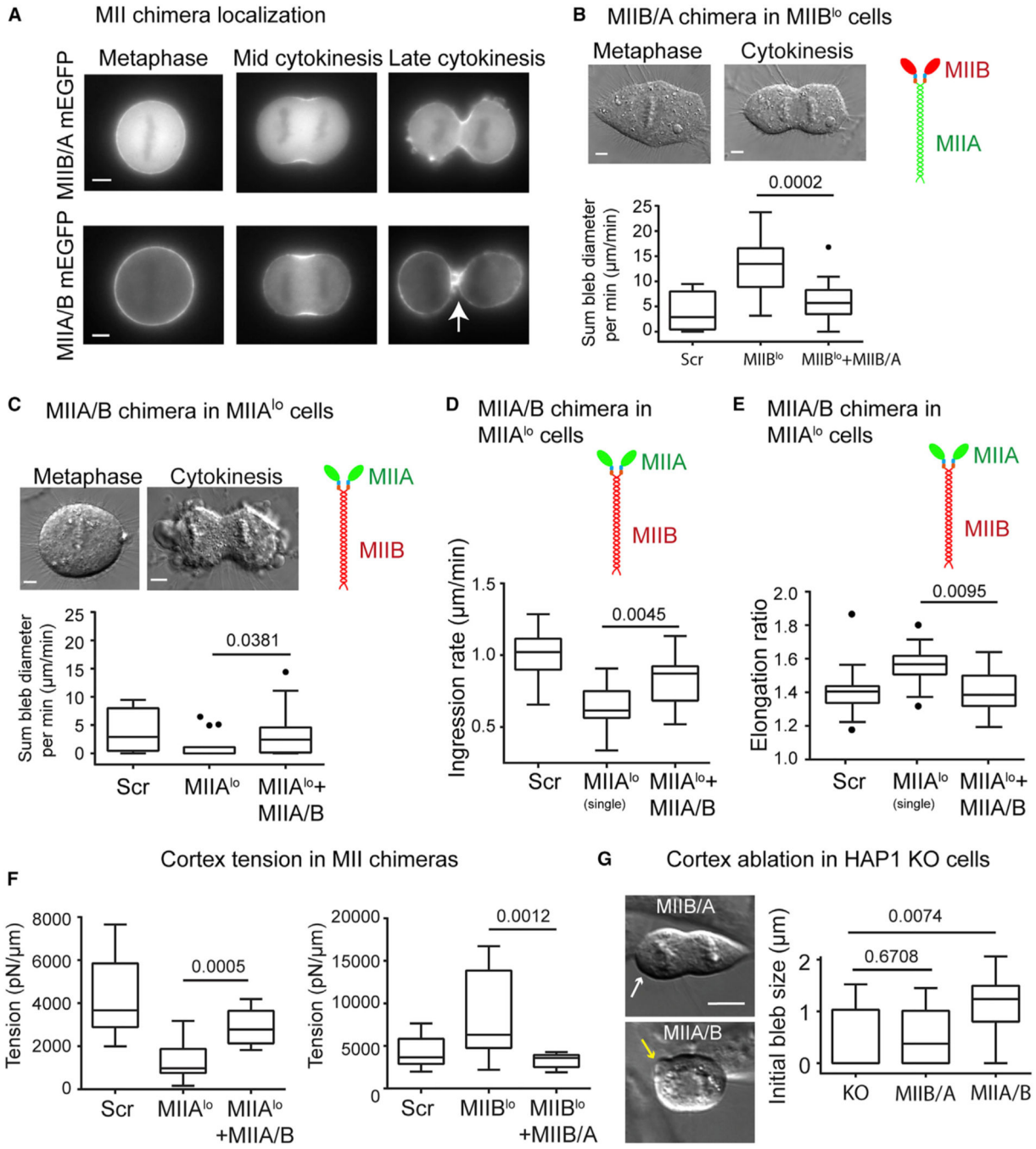

Figure 5. Motor Domains Determine the Contribution of MII Paralogs to Cortical Contractility

(A) Localization of MIIB/A-mEGFP and MIIA/B-mEGFP chimera in MIIB^{lo} and MIIA^{lo} cells, respectively. Arrow indicates enrichment of MIIA/B at the equatorial cortex during late cytokinesis.

(B) MIIB^{lo} cell expressing MIIB/A chimera at metaphase and cytokinesis. Tukey plots of blebbing events in MIIB/A-expressing cells compared to Scr and MIIB^{lo} (single siRNA). n = 16 MIIB^{lo} +MIIB/A cells, N = 3 experiments. The Scr and MIIB^{lo} (single) datasets are the same as in Figure 2B and are only shown for comparison.

(C) MIIA^{lo} cell expressing MIIA/B chimera at metaphase and cytokinesis. n = 16 MIIA^{lo} +MIIA/B cells, N = 3 experiments. The Scr and MIIA^{lo} (single) datasets are the same as Figure 2C and are only shown for comparison.
(D) Cleavage furrow ingression rates using DIC comparing MIIA^{lo} cells expressing MIIA/B chimera. n = 16 MIIA^{lo} +MIIA/B cells, N = 3 experiments. The Scr and MIIA^{lo} (single) datasets are the same as Figure 1F and are only shown for comparison.
(E) Pole-to-pole elongation ratios for MIIA^{lo} cells expressing MIIA/B chimera. n = 12 MIIA^{lo} +MIIA/B cells, N = 3 experiments. The Scr and MIIA^{lo} (single) datasets are the same as Figure S3 and are only shown for comparison.
(F) Cortex tension in MIIB/A and MIIA/B chimeras using micropipette aspiration. n = 14 MIIA^{lo} +MIIA/B- and 10 MIIB^{lo} +MIIB/A-expressing cells, N = 4 experiments. The Scr, MIIA^{lo}, and MIIB^{lo} datasets are the same as in Figure 4B and are only shown for comparison.
(G) Initial bleb size following ablation in HAP1 KO cells. n = 8 MIIB/A- and 18 MIIA/B-expressing cells, N = 3 experiments. Yellow and white arrows denote formation or absence of a bleb, respectively. The control KO dataset is the same as Figure 4G and is only shown for comparison.
Scale bars, (A and G) 10 μm; (B and C), 5 μm. Solid circles represent outliers. p values stated over graphs.

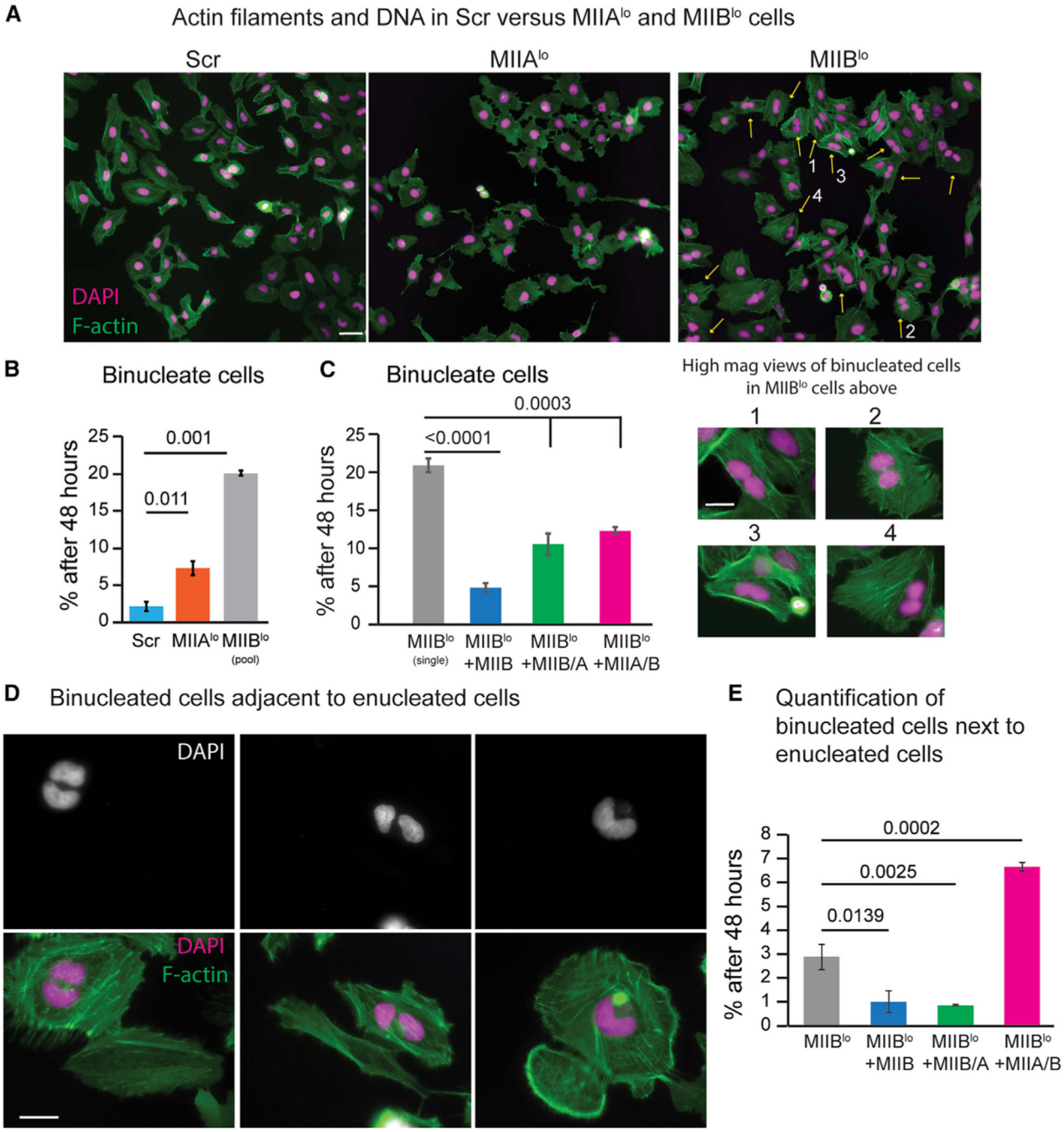

Figure 6. MIIB Depletion Leads to Increased Binucleation

(A) Scr, MIIA^{lo}, and MIIB^{lo} cells 48 h post re-plating, showing F-actin (green) and nuclei (magenta). Yellow arrows denote binucleated cells. (Inset) Higher magnification examples, 1–4.

(B) Binucleate cells 48-h post plating in Scr versus MIIA^{lo} (pooled siRNA) or MIIB^{lo} (pooled siRNA) cells. n > = 1,000 cells each, N = 3 experiments.

(C) Binucleate cells 48-h post plating in MIIB^{lo} (single siRNA) versus MIIB^{lo} cells expressing MIIB, MIIB/A, or MIIA/B. n = 760 MIIB^{lo} (single), 584 MIIB-expressing, 464 MIIB/A-expressing, and 347 MIIA/B-expressing MIIB^{lo} cells, N = 3 experiments.
(D) Representative binucleated MIIB^{lo} cells adjacent to enucleated cells.
(E) Binucleated cells adjacent to an enucleated cell, as a fraction of total number of cells.
Scale bars, (A) 50 μm; (inset), 25 μm; (D) 25 μm. Error bars represent standard error of the mean. p values stated over graphs.

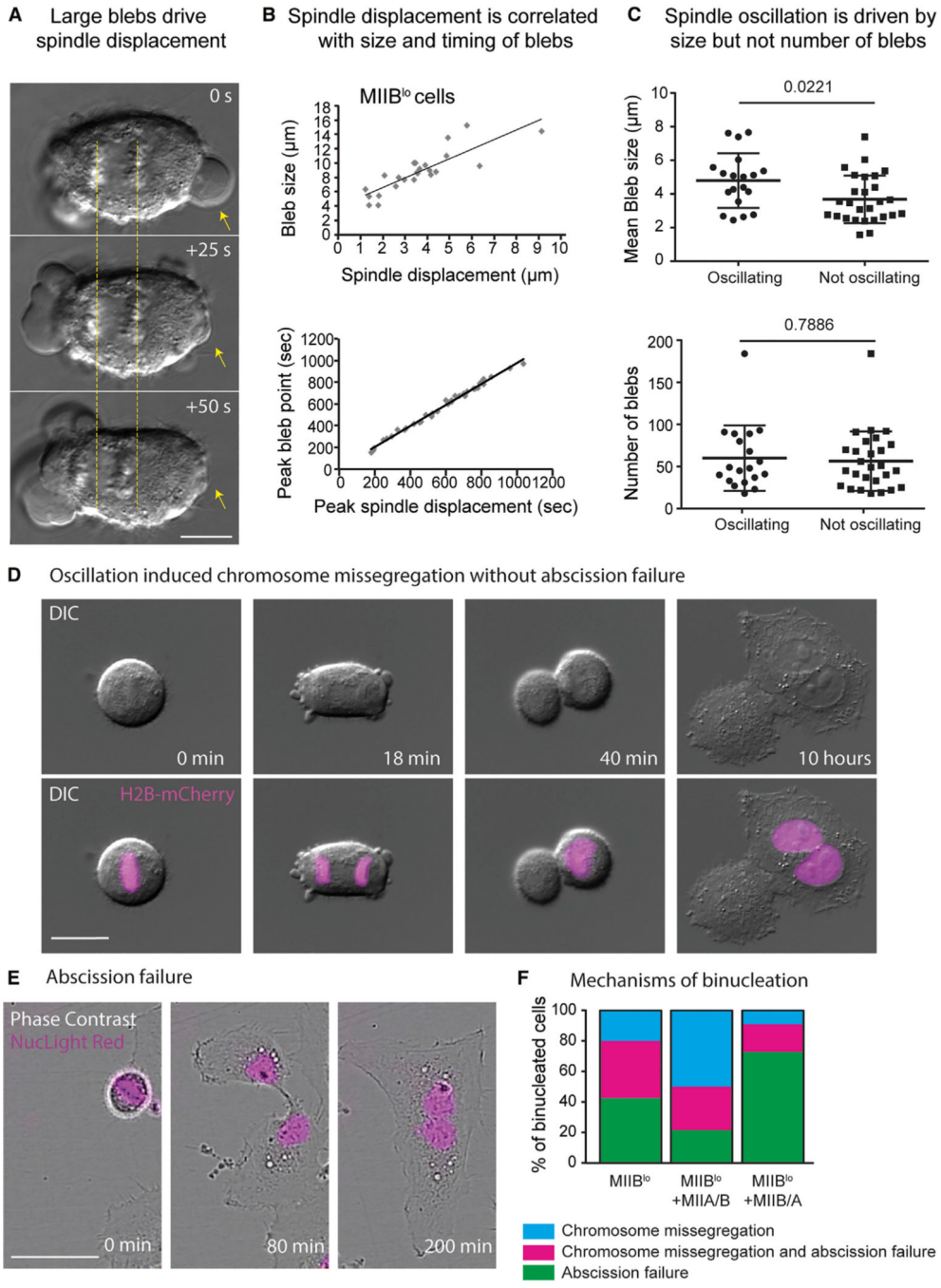

Figure 7. Loss of MIIB Drives Binucleation through Two Distinct Mechanisms

(A) Time montage showing displacement of the chromosomes (dotted yellow lines) with the retraction of a large bleb (yellow arrow) in a MIIB^{lo} cell.

(B) Correlation of spindle displacement with the size and timing of blebbing events. Each data point represents a bleb/displacement event plotted over 3 experiments.

(C) Comparison of oscillating versus non-oscillating cells with respect to bleb size and number of blebbing events. Each data point represents a cell. n = 36 cells,N = 6 experiments.

(D) Representative time montage of spindle oscillation-induced chromosome missegregation upon MIIB depletion.
(E) Representative time montage showing abscission failure upon MIIB depletion. See Figure S7B for extended time montage. The ROI used to create the montage was moved to keep the cells centered in the field of view.
(F) Relative proportions of the modes of binucleation upon MIIB depletion. n = 40 $MIIB^{lo}$, 11 $MIIB^{lo}$+MIIB/A, and 14 $MIIB^{lo}$+MIIA/B binucleation events.
Error bars in (C) represent standard deviation. Scale bars, 10 μm (A); 20 μm (D); 50 μm (E). p values stated over graphs.

KEY RESOURCES TABLE

REAGENT or RESOURCE	SOURCE	IDENTIFIER
Antibodies		
Rabbit polyclonal IgG anti-NMIIB	Cell Signaling Technology	3404S; RRID: AB_1264210
Rabbit monoclonal IgG anti-NMIIB	Cell Signaling Technology	8824S; RRID: AB_11217639
Rabbit polyclonal IgG anti-NMIIA	BioLegend	P909801; RRID: AB_2565100
Goat anti-rabbit IgG AlexaFluor 488	Thermo Fisher Scientific	A-11008; RRID: AB_143165
Goat anti-rabbit IgG AlexaFluor 568	Thermo Fisher Scientific	A-11011; RRID: AB_143157
Bacterial and Virus Strains		
Biological Samples		
Chemicals, Peptides, and Recombinant Proteins		
NucLight Rapid Red	Essen Biosciences	4717
Blebbistatin	Sigma	B0560
Fugene 6	Promega	E-2691
Lipofectamin 2000	Thermo Fisher Scientific	11668027
AlexaFluor 488 Phalloidin	Thermo Fisher Scientific	A12379
AlexaFluor 568 Phalloidin	Thermo Fisher Scientific	A12380
Critical Commercial Assays		
QIAprep spin Miniprep Kit 250	QIAGEN	27106
Experimental Models: Cell Lines		
HeLa	American Type Culture Collection	CCL-2
Cos-7	Gift from Jeniffer Lipincott Shwartz	N/A
M2	Gift from Matthew Tyska	N/A
H9	WiCell Research Institute	WA09
HAP1 Parental	Horizon Discovery	C631
HAP1 myh9 KO	Horizon Discovery	HZGHC00108

REAGENT or RESOURCE	SOURCE	IDENTIFIER
Oligonucleotides		
SmartPool siRNA against myh9	GE Dharmacon	E-007668-00-0005
SmartPool siRNA against myh10	GE Dharmacon	E-023017-00-0010
Individual siRNA against myh9	GE Dharmacon	A-007668-13-0005
Individual siRNA against myh10	GE Dharmacon	A-023017-15-0005
Recombinant DNA		
siRNA resistant NMIIB (N-terminal) mEGFP	This study	N/A
siRNA resistant NMIIB/A (N-terminal) mEGFP	This study	N/A
NMIIA/B (N-terminal) mEGFP	Gift from Miguel Vicente-Manzanarez	N/A
NMIIB/A (N-terminal) mEGFP	Gift from Miguel Vicente-Manzanarez	N/A
NMIIB (N-terminal) mEmerald	Addgene	54192
NMIIA (N-terminal) mApple	Addgene	54929
NMIIB (N-terminal) mEGFP	Addgene	35691
NMIIA (N-terminal) mEGFP	Addgene	11347
Software and Algorithms		
Fiji (ImageJ)	NIH (freely available)	https://imagej.net/Fiji/Downloads
Measurement of cortex tension using micropipette aspiration MATLAB script	This study	N/A